Quantum parity detectors: A qubit-based particle-detection scheme with meV thresholds for rare-event searches

K. Ramanathan,[1,*] B. J. Sandoval,[2] J. E. Parker,[2] L. M. Joshi,[3] A. D. Beyer,[4] P. M. Echternach,[4] S. Rosenblum,[3] and S. R. Golwala[2]

[1]*Department of Physics, Washington University in St. Louis, St. Louis, Missouri 63130, USA*
[2]*Department of Physics, California Institute of Technology, Pasadena, California 91125, USA*
[3]*Department of Condensed Matter Physics, Weizmann Institute of Science, Rehovot, Israel*
[4]*Jet Propulsion Laboratory, California Institute of Technology, Pasadena, California 91109, USA*

(Received 12 September 2025; revised 17 January 2026; accepted 13 April 2026; published 1 May 2026)

The next generation of rare-event searches, such as those aimed at determining the nature of particle dark matter or measuring fundamental neutrino properties, will benefit from particle detectors with thresholds at the meV scale, 100–1000× lower than currently available. Quantum parity detectors (QPDs) are a class of proposed quantum devices, extending recent work on superconducting qubit sensors, that exploit the fingerprints of single quasiparticle tunneling across a coherent weak link as their detection concept. As envisioned, phonons generated by particle interactions within a crystalline substrate cause an eventual quasiparticle cascade within a surface-patterned superconducting qubit element. This process alters the fundamental charge parity of the device in a binary manner, which can be used to deduce the initial properties of the energy deposition. This work lays out multiple resonator-coupled readout schemes depending on qubit architecture, provides an analytic formulation for reconstructing sensor energies, and details strategies for multiplexing large arrays of sensors. We further compute the sensitivity of QPDs and detail an R&D pathway to demonstrating sub-eV energy deposit thresholds.

DOI: 10.1103/kqd2-spb1

I. INTRODUCTION

A key science requirement for the next generation of rare-event searches, such as those looking for very light particle dark matter or expanding neutrino measurement regimes [1,2], is the ability to identify energy deposits $\ll$eV within a macroscopic [$\mathcal{O}$(g)] target mass. For example, theoretically well-motivated particle dark matter candidates with $\mathcal{O}(10\text{–}10^4)$ keV c^{-2} masses may interact with an atomic target and kinematically transfer only $\mathcal{O}(1\text{–}10^3)$ meV [3]. Further complicating this picture is that, as the interaction energy (momentum) scale drops below the $\sim$eV ($\sim$keV c^{-1}) level in common crystalline target materials, it is predominantly only collective excitations that are created, the most common of which are phonons (lattice vibration quanta) [4]. In the case of a dark matter candidate coupled to the standard model through an electromagnetic current (e.g., dark photons), interactions with an ionic crystal can likewise produce optical phonons with energies down to $\mathcal{O}(10\text{–}10^2)$ meV

*Contact author: karthikr@wustl.edu

Published by the American Physical Society under the terms of the Creative Commons Attribution 4.0 International license. Further distribution of this work must maintain attribution to the author(s) and the published article's title, journal citation, and DOI.

[5]. Transition edge sensors [6] have demonstrated the lowest thresholds for detection of phonons, at the $\mathcal{O}(100)$ meV to eV level [7–11], and kinetic inductance detectors (KIDs) are on a similar trajectory [12–14]. However, it remains an outstanding particle physics community priority to demonstrate *single-phonon-sensitive detectors* as tools in the search for new physics [3].

Concurrently, the past decades have seen rapid progress in the field of superconducting qubits for quantum information science (QIS) [15,16]. These computing building blocks have been shown to be affected by environmental radioactivity, producing correlated errors across an entire wafer [17], induced by charge and phonons produced within the substrate. An active area of QIS R&D is in mitigating these effects by engineering phonon or quasiparticle absorbers and sinks, and gap engineering [18–21].

Crucially, the relevant energy scales of the physical phenomena affecting qubit coherence are matched to the particle physics requirements discussed above. For example, in a common qubit material like aluminum with a superconducting Cooper pair-breaking gap of $2\Delta \approx 400\,\mu\text{eV}$, any resultant quasiparticle (broken Cooper pair) from phonon absorption can tunnel across the Josephson junction at the heart of the circuit. This tunneling process has a fingerprint, modifying the energy level structure of the qubit and possibly decohering it [22–24].

Quantum capacitance detectors (QCDs) [25,26], based on single Cooper-pair box (CPB) qubit designs [15], exploit this quasiparticle tunneling process for far-infrared radiation detection, and they have since demonstrated the ability to count 1.5 THz photons [27] using an rf-based readout scheme that lends itself to easy multiplexing, with over 400 QCDs chained on a single feedline [28]. It is natural to consider whether such sensors can be repurposed as generic phonon-mediated detectors for rare-event searches. Complementary work by Linehan *et al.* [29] has investigated the efficacy of using correlated errors in conventional transmon qubits to build phonon-sensitive detectors, but concludes that energy resolutions are limited to the $\mathcal{O}(10)$ eV level. The SQUAT concept of Fink *et al.* [30] dramatically reimagines a qubit's architecture, directly coupling it to the rf feedline, while still measuring changes to charge parity as with the seminal QCD work. The SQUAT scheme, while promising, requires coupled sensor/readout design, use of quantum-limited amplifiers, and trade-offs in sensor bandwidth and signal-to-noise ratio (SNR). Further, the direct feedline coupling is potentially susceptible to an aggravated excess quasiparticle density, arising from hypothesized thermal or multiphoton processes observed in qubits [31] and resonators [32,33]. This note lays out the intermediate approach of a resonator-coupled charge-parity-sensitive pair-breaking detector, which we term quantum parity detectors (QPDs). This architecture considers phonon-sensitive CPB designs as well as offset-charge-sensitive (OCS) transmons [34,35], platforms that are well studied in the literature. Section II outlines the detector concept. Section III describes relevant physical principles along with the readout mechanism, including providing for an analytical formulation of tunneling rates that allows for direct determination of device sensitivity. Section IV details the estimated performance along with cataloging expected noise sources. Finally, Sec. IV D outlines future choices and challenges to be addressed.

II. DEVICE CONCEPT

A schematic overview of the device concept is given in Fig. 1, following well-established phonon-mediated quasiparticle trapping designs such as Ref. [6]. A rare-event interaction such as that of a dark matter particle scattering within the substrate creates an energy deposit E_{dep} that will result in the production and propagation of phonons. The substrate is a high-resistivity, macroscopically thick crystal, typically $\mathcal{O}(\text{g})$ in mass, with silicon, germanium, and sapphire (Al_2O_3) being common choices for rare-event experiment architectures [36,37]. The QPD portion consists of two superconducting pads patterned on the substrate surface coupled by a Josephson junction of an $\mathcal{O}(100)$ nm side length [38], akin to a traditional qubit design [35,39]. Depending on whether it is an OCS- or QCD-style sensor, with heritage from transmon or CPB qubits, respectively, the pads can be symmetrically large (*absorber-absorber*) or asymmetric (*absorber-island*). The produced phonons impinge on and can be absorbed by the pads, breaking Cooper pairs and creating

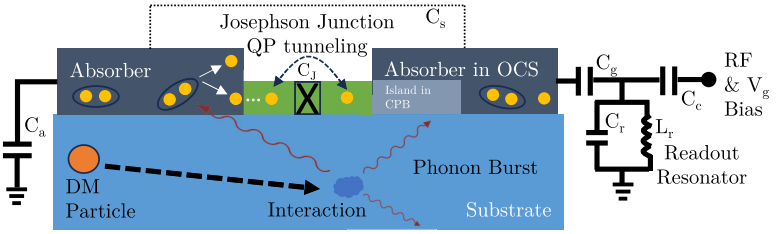


FIG. 1. Schematic of the operating principle of both QPD styles. A quasiparticle trapping region containing the Josephson junction (green) is sandwiched either by large superconducting absorbers (OCS, gray) or by an absorber and small island (CPB, light gray). The structure is embedded in a resonant readout circuit, with identified circuit terms, and patterned on the surface of a crystalline substrate (blue).

quasiparticles. These absorber quasiparticles diffuse to and are trapped in an overlapping smaller volume, lower superconducting gap region called the trap (also known as the junction leads in qubit-specific literature), and dramatically change the quasiparticle density near the Josephson junction. This modulation of quasiparticle density, δn_{qp}, and subsequent rapid tunneling back and forth across the junction, can be sensed via a quantum-mechanical interaction with the coupled readout resonator of bare frequency ω_r $(= 1/\sqrt{L_r C_r} = 2\pi f_r)$. The absorber is made of $\mathcal{O}$(100s) nm (e.g., 500 nm), relatively thick aluminum (due to its capability to absorb phonons and diffuse quasiparticle efficiently), while the junction is to be made of an $\mathcal{O}(100)$ nm thick, low-gap material (such as hafnium) for the purpose of efficient quasiparticle trapping [40,41]. Hafnium is a promising candidate as tunnel junctions have been successfully demonstrated in the literature [42,43], though not as part of a qubit architecture.

Proposed layouts of the two types of QPDs can be seen in Fig. 2, highlighting the discussed elements of the absorber, island, resonator, readout feedline, and Josephson junction.

Charge qubits (which include CPBs and transmons) are superconducting circuits engineered to have addressable "charge" basis states—Simplistically, their properties are determined by the

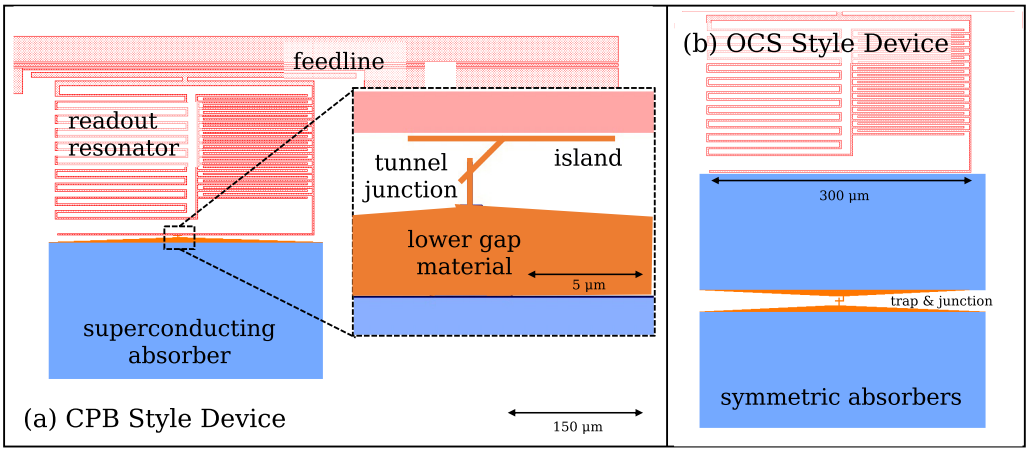


FIG. 2. Stylized mask layouts of QPDs. Items in red are made of a high-gap material (e.g., Nb or Ta), used for the feedline and resonator. Blue represents an intermediate-gap material (e.g., Al) for the phonon absorber. Orange highlights the low-gap material (e.g., Hf) trap and junction. (a) QCD-derived sensor, with large absorber connected to small island. We note the potential use of a lower-gap (than the absorber) material to connect the large absorber to the tunnel junction (and the island) to enable quasiparticle trapping and multiplication. (b) Resonator and absorber region for an OCS design, with mostly identical components except larger, symmetric pads that introduce a shunt capacitance. Trapping may be implemented on both sides of the junction.

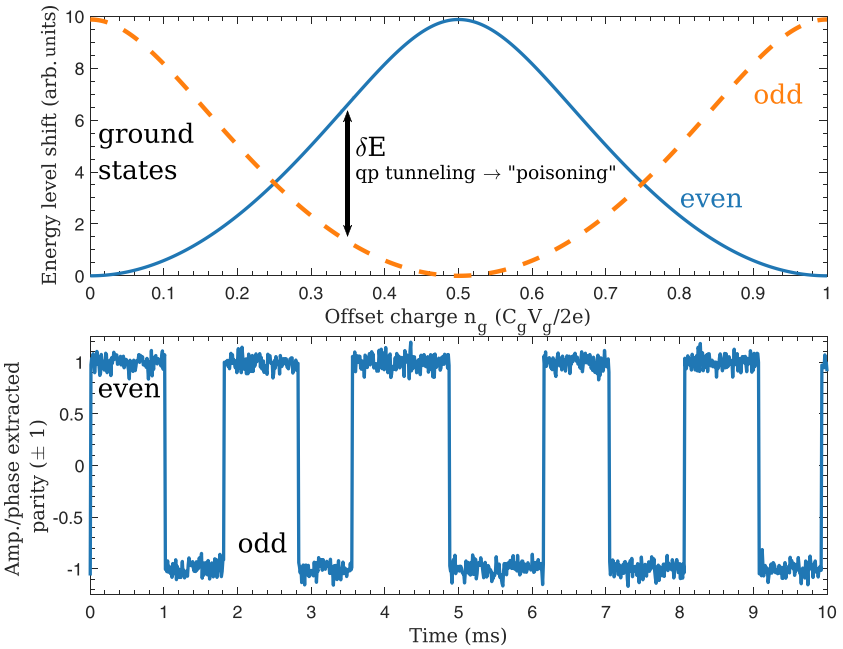


FIG. 3. Top: Stylized ground-state energy level shifts for a charge qubit, showing the different curves for even and odd number of charges on the island, with δE difference in energy. A quasiparticle tunneling event shifts the qubit from one state to the other. Bottom: Simulated resonator telegraph signal from background quasiparticle tunneling events. Each tunneling event causes a charge parity shift and thus an amplitude/phase change in the resonator signal, and this rate is proportional to the quasiparticle density within the absorbers.

number of Cooper pairs present on an isolated island [15,35,44]. As will be elucidated in Sec. III C, charge qubits can be treated as anharmonic quantum oscillators, reducible to a two-level quantum system, and thus have found great use as building blocks for quantum computing [45,46]. However, due to their environmental sensitivity, these schemes can be affected by the incoherent tunneling of quasiparticles across the Josephson junction. The ground-state energy of the qubit is actually a sinusoidal function of the offset charge, n_g, on the island, as shown in Fig. 3 (top). The addition of a single quasiparticle can be interpreted as a change in n_g by 0.5, causing the qubit to switch between the "odd" and "even" curves, with a difference in energy of δE. Hence, it is said that addition or removal of a quasiparticle changes the "charge parity" of the system [34]. Even in the case of very low temperature operation, with a thermally suppressed quasiparticle population, nonequilibrium quasiparticles from other sources pose this risk of quasiparticle poisoning [48], potentially ruining quantum coherence. Regardless of QPD type, a microwave resonator with bare resonant frequency ω_r can be capacitively coupled to the qubit to monitor the charge parity [47]. Any excess population of nonequilibrium quasiparticles created by phonon absorption can tunnel across the junction and thus be sensed by each tunneling event's impact on ω_r, with the tunneling rate ($\mathcal{O}(1)$ kHz μm^3) proportional to this quasiparticle density. The excess rate of charge parity transitions should thus be proportional to the original substrate energy deposition, providing a basis for using QPDs for particle detection [27]. Figure 3 (bottom) shows an example of the expected resonator response to charge parity shifts, called a telegraph signal. We consider even charge parity to be zero or an even number of quasiparticles (with odd being the complement) to have tunneled across the barrier. Additionally, an applied voltage bias V_g, adjusted with the aid of a gate capacitor C_g, allows for tuning of the gate charge operating point to maximize the observed charge parity switch signal.

In the QPD scheme, the underlying qubits are always operated in their ground state, requiring no complex state manipulation. Additionally, the sensors do not interact with each other. Thus, QPDs have the added benefit of easy multiplexability, as each qubit can be coupled to a readout resonator of a slightly different resonant frequency. The expected maximal dispersive shift of a GHz resonator due to a charge parity switching event will be $\mathcal{O}(100)$ kHz for OCS-style devices and $\mathcal{O}(10)$ MHz for CPB-style devices. See Sec. III E for more details on the expected parity frequency shift. Furthermore, even the lower bound parity frequency shift is a significant fraction of the resonators' FWHM f_r/Q for a loaded quality factor $Q_r \sim 10^4$. The frequency noise (while in either the even or odd states) is nominally expected to be $\mathcal{O}(100)$ Hz [49,50]; hence, we expect the even and odd states to be easily resolvable. In other words, any reasonable rf probe will be able to continuously distinguish even versus odd states. There is, however, the added complexity of having to tune the gate charges for each QPD, due to differences between QPDs arising from charge inhomogeneities and associated drifts. For a single QPD, this problem can be overcome by actively monitoring n_g via the size of observed charge parity shifts (or other related variables, such as changes in the qubit transition frequency) and adjusting the voltage gate bias, a technique already used in qubit systems [51]. For multiplexed systems, we may continuously sweep the gate bias voltage through one full period of gate charge. A tunneling event will then interrupt the periodic output signal differently depending on whether the device utilizes an OCS or CPB qubit. A full discussion of the expected response when sweeping the gate voltage is given in Sec. III E.

III. DEVICE PHYSICS

An energy deposition into the substrate generates a phonon event whose absorption into a superconducting film on the surface engenders a pulselike time-varying change in the quasiparticle density in the absorber $\delta n_{\mathrm{qp,abs}}(t)$. Nominally, there are multiple timescales that need to be considered for both phonons and quasiparticles, including cyclic transfer of energy between both channels [52]. In tandem, there are a string of efficiencies modulating the transfer of energy between each step of the overall process, for example, factoring in phonon losses to surface-mediated down-conversion or efficiency of quasiparticle trapping into the trapping region. Various references have cataloged said efficiencies and timescales [53,54], but crucially there is no singular literature model that reproduces observed pulse shapes across various detector modalities. Rather, it seems that experiment-specific factors of material selection, geometry, mounting, film properties, application of a bias field, etc. all impact the detector response and must be disentangled empirically. As such, we limit ourselves to simplified models for determining $\delta n_{\mathrm{qp,abs}}$ and $\delta n_{\mathrm{qp,trap}}$ (the quasiparticle density in the trap), useful to get a flavor of detector operation. We first consider the expected efficiency of capturing phonon energy by the absorber pads and then follow with a discussion on the expected efficiency of quasiparticle number within the trap, visually summarized in Fig. 4.

A. Phonon response and efficiencies

Following the description in Ref. [55], the initial burst of phonons will be around the Debye frequency of $\mathcal{O}(10)$ THz. Decay and scattering processes cause these relatively high-frequency phonons to down-convert within a few microseconds to phonons that propagate quasidiffusively with a speed less than the crystal's sound speed. Once the phonon energies are low enough (still meV and thus athermal for a subkelvin substrate), the mean free path exceeds the crystal dimensions. They travel ballistically at the sound speed and are subject primarily to reflections at the bare crystal surfaces or absorption at interfaces between the crystal and other materials (thin films and mounting points). Typical optical branch phonon energies in commonly considered crystalline substrates are of $\mathcal{O}$(10–100) meV with the high tail of acoustic phonons ($k_B T_{\mathrm{Debye}}$) reaching this level.

To begin understanding the transfer of energy within the detector, we first model the fraction of the deposited phonon energy E_{dep} that enters the absorber, called the phonon collection efficiency η_{ph} in some literature (e.g., Ref. [56]). Using the prescription Ref. [57] sketches out, η_{ph} can be

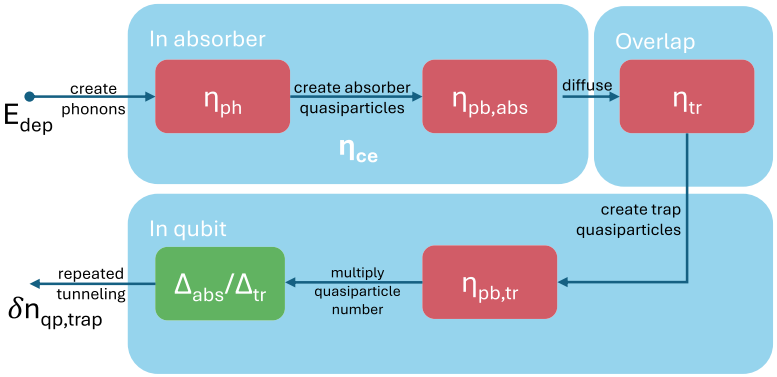


FIG. 4. Stylized chart showing the string of efficiencies that modulate the initial substrate deposit E_{dep} into a changing quasiparticle density, $\delta n_{\mathrm{qp,trap}}$, near the junction region of the QPD. The first four efficiencies reduce either the available energy or quasiparticle population to be sensed, while the final act of trapping induces a quasiparticle multiplication. Specific details of absorber efficiencies can be found in Sec. III A, while quasiparticle physics in the overlap and trap region is touched on in Sec. III D.

maximized via the heuristic

$$\eta_{\mathrm{ph}} \sim f_{\mathrm{surf}} f_{\mathrm{abs}} N_{\mathrm{surf}} (1 - f_{\mathrm{loss}}) \leqslant 1. \tag{1}$$

f_{surf} is the instrumented fraction of the substrate's surface, f_{abs} is the probability of absorption per interaction with the surface sensors, N_{surf} is the number of phonon surface encounters before thermalization below the absorber gap, and f_{loss} is a parasitic loss term (e.g., from phonon down-conversion and losses to chip mounting). Average phonon sound speeds of km s^{-1} and nominal lifetimes against anharmonic down-conversion of $\mathcal{O}(1)$ ms suggest $N_{\mathrm{surf}} > 10^3$ for millimeter-thick substrates. With $f_{\mathrm{abs}} > 0.1$ for $\mathcal{O}(100)$ nm thick aluminum on silicon (Al has a 1.6 μm pair-breaking length [52] and sound-speed mismatch limits the phonon transmittance to <0.9), f_{surf} as low as a few percent may, optimistically, be sufficient for complete energy collection. Work by Ren *et al.* [56] provides evidence that $\eta_{\mathrm{ph}} > 0.95$ is achievable in a phonon-mediated detector context, though with almost complete surface coverage, while recent results from Ref. [58] detail $\eta_{\mathrm{ph}} \sim 0.3$ overall with a low 1% surface coverage, both for Si substrates. These results are broadly in line with the presented formalism, though care must be taken to properly understand the f_{loss} term across different architectures.

As Fig. 2 shows in light red, our QPD designs have feedline and resonator structures that may prove lossy to phonons. Parasitic losses to these inactive/passive surface metal films ("dead metal") and mountings must not unintentionally degrade the phonon population and lifetime. The exact form of f_{loss} is an open question, but recent work by Wen [59] suggests that dead metal losses may scale with the *volume* of the loss channel and that a material like niobium, commonly used to pattern secondary planar structures, is about ∼10% as efficient as aluminum in absorbing Si substrate athermal phonons. As such, one can plausibly model $f_{\mathrm{loss}} \sim \Sigma_i \xi_i V_i / V_{\mathrm{metal}}$ as a sum over all loss channels with loss volumes V_i (an effective volume when modeling losses to the mounting), total surface metal volume V_{metal}, and a relative lossiness measure ξ_i. Additionally, the substrate-absorber transmittance must be high enough to not degrade f_{abs}.

Once the phonons have entered the film, the next source of energy loss is incurred as a finite fraction of the phonon energy in the absorber is converted into quasiparticles (due to quasiparticles emitting sub-Δ_{abs} (the superconducting gap of the absorber) phonons as they relax to the gap after creation). This phonon-to-quasiparticle pair-breaking efficiency in the absorber is parametrized by $\eta_{\mathrm{pb,abs}}$. Simulation work of *photon* absorption in a thin-film superconductor suggests a general range of $\eta_{\mathrm{pb}} \sim 0.4$–$0.6$ [60,61]. It is reasonable to assume a similar $\eta_{\mathrm{pb,abs}}$ for phonon absorption.

We can combine the phonon absorption and pair breaking into a single dimensionless *total energy collection efficiency* [13,62],

$$\eta_{ce} = \eta_{pb,abs}\eta_{ph} = N_{sens}V_{abs}\Delta_{abs}\delta n_{qp,abs}/E_{dep}, \tag{2}$$

that helps directly translate from deposited energy E_{dep} to the produced quasiparticle number $V_{abs}\delta n_{qp,abs}$ (for absorber volume V_{abs} and quasiparticle density $\delta n_{qp,abs}$). N_{sens} is the number of sensors populating the surface and maps to changes in f_{surf} from Eq. (1), assuming equal phonon energy splitting.

To quantify phonon absorption for a representative QPD design, we examine the case of a 1 cm $\times$ 1 cm $\times$ 0.1 cm Si chip. A centimeter-long minimal niobium coplanar waveguide (CPW) feedline [63] has an effective volume of about 35 000 μm^3. A fairly standard lumped element resonator, akin to the one shown in Fig. 2, represents a small 450 μm^3 increase to that value per QPD (the feedline ground plane is reduced at that location to increase the coupling quality factor). Both are dwarfed, in arrays of multiple QPDs, by the expected 60 000 μm^3 volume of a *single* QPD's absorber pads.

A design with a 4% area coverage requires a 2.5 cm feedline and about 50 QPDs. We can estimate η_{ce} by comparing this design to Ref. [64], which details the performance of a mixed Al/Nb phonon-mediated KID. They present a raw $\eta_{ce} \approx 0.009$ in a mixed Al/Nb device, but their f_{surf} is very small $\sim$0.001 7 and f_{loss} is estimated to be $>$0.95, with phonons lost to both a large volume of Nb and the mounting. Scaling f_{surf} to 0.04 and eliminating all the Nb except for the feedline yields a predicted η_{ce} of about 0.3, dominated by losses to the mounting ($f_{loss} \sim 0.35$). A similar survey of the broader literature on phonon-mediated detectors coupling sapphire, silicon, and germanium substrates to both thick- [$\mathcal{O}$(100) nm] and thin-film [$\mathcal{O}$(10) nm] aluminum absorbers yields an estimate of $\eta_{ce} \sim$ 0.1–0.4 [13,56,58,65–67] for our thick-film, percent-level surface coverage absorber scenario.

Optimizing the efficiencies presented in this section will largely rely on proper engineering. For instance, resonator architectures with parallel-plate capacitors [68], which have already been demonstrated for transmon readout, can possibly reduce resonator volumes down to a negligible $\sim$75 μm^3 per QPD over the feedline volume with an accompanying small footprint. In principle, the issue of dead metal can be rendered entirely moot by adopting a flip-chip architecture [69,70], where all qubit readout and control architecture is moved to a *separate* chip located a few micrometers above the qubits and is only capacitively or inductively coupled. In addition, work by Romani [71] has demonstrated the ability to hang chips using wirebonds, which presents an attractive strategy to mitigate any losses to the mounting.

B. Quasiparticle response and efficiencies

Once the quasiparticles are produced within the absorber and diffuse toward the junction, they can recombine before they become trapped in the lower-gap region. Hence, we expect only a fraction of the initially generated quasiparticles to actually become trapped, parametrized by the trapping efficiency η_{tr}. To estimate η_{tr}, we use a one-dimensional (1D) analytic diffusion model [72], described in detail in Appendix B. We find that this term is expected to be $\mathcal{O}(0.1)$ for $\mathcal{O}$(100 μm) absorber lengths, $\mathcal{O}$(10 μm) trap lengths, and $\mathcal{O}$(100 nm) thick films.

A quasiparticle becomes trapped once it enters the lower-gap region and decays in energy to Δ_{tr} (the superconducting gap of the trap) by phonon emission. Because we have $\Delta_{abs} \gg \Delta_{tr}$, the phonon cascade generated as the quasiparticle relaxes to the lower gap can break Cooper pairs and generate more quasiparticles, yielding a quasiparticle multiplication effect. The upper bound of this multiplication is roughly equal to Δ_{abs}/Δ_{tr} [40,73], where we have made the approximation that all absorber quasiparticles entering the trap have energy Δ_{abs}, which is reasonable given how quickly excited quasiparticles decay to near Δ_{abs} by phonon emission [52]. In the pair-breaking processes occurring within the trap, we will once again lose a fraction of energy to sub-Δ_{tr} phonons emitted as the newly created quasiparticles relax to the gap. Hence, we once again must include a pair-breaking efficiency $\eta_{pb,tr}$, expected to be similar in magnitude to $\eta_{pb,abs}$.

Assuming again an equal split of energy across N_{sens} number of sensors, we can now estimate the maximum number of quasiparticles N_{qp}^{r} produced and trapped in the lower-gap region near the junction of a single QPD as

$$\begin{aligned} N_{\text{qp}}^{r} &= \frac{E_{\text{dep}}}{N_{\text{sens}}\Delta_{\text{abs}}}\eta_{\text{ph}}\eta_{\text{pb,abs}}\eta_{\text{tr}}\eta_{\text{pb,tr}}\frac{\Delta_{\text{abs}}}{\Delta_{\text{tr}}} \\ &= \frac{E_{\text{dep}}\eta_{\text{ce}}\eta_{\text{tr}}\eta_{\text{pb,tr}}}{N_{\text{sens}}\Delta_{\text{tr}}} = \frac{E_{\text{abs}}\eta_{\text{tr}}\eta_{\text{pb,tr}}}{\Delta_{\text{tr}}}, \end{aligned} \tag{3}$$

having strung together factors from our preceding discussion in Sec. III A. We note that the decrease in quasiparticle number with increasing N_{sens} is in part balanced by the increase in η_{ce} with more sensors. For future convenience in Sec. IV C, where we discuss intrinsic sensor resolutions, we have introduced E_{abs} in the final expression, as the energy effectively absorbed and converted into quasiparticles within the absorbers of a single QPD.

Now that we have modeled the expected quasiparticle production within the trapping region, we proceed to construct a simplified $\delta n_{\text{qp,trap}}(t)$ model of the dynamic change in quasiparticle density within the trap. We introduce two time constants: a quasiparticle injection timescale τ_{inj}, which characterizes how long quasiparticles take to enter into the trap, and τ_{qp}, the recombination time constant within the film [52,53,74]. τ_{inj} subsumes the expected quasiparticle lifetime within the absorber, phonon time constants related to how long $>2\Delta_{\text{abs}}$ phonons are present in the substrate to break pairs in the absorber films, and diffusion-related time constants. We intuit that τ_{inj} will be set by the longest of these constants. To provide a scale, literature measurements of τ_{qp} range from 0.1 to 10 ms in Al [13,75–78], depending on the quiescent quasiparticle density n_0. Qubit and related superconducting systems report $n_0 \sim 0.1$–$1\ \mu\text{m}^{-3}$ (e.g., Refs. [51,79,80]), which would correspond to $\tau_{\text{qp}} \gg$ ms for a standard generation-recombination model with Al recombination constant $R \approx 10\ \mu\text{m}^3\ \text{s}^{-1}$ [81]. We assume a vanishing rise time for the phonon population, neglecting the time it takes for the phonons produced by the energy deposition to become an approximately spatially homogeneous population in the substrate, because that rise time is only a few times the $\mathcal{O}(\mu\text{s})$ sound travel time for the considered substrates. As cataloged by Ref. [57], we expect phonon absorption lifetimes, τ_{abs}, of $\mathcal{O}(\text{ms})$. Overall, we can write and solve the forced differential equation of a single sensor (see Appendix A for specifics) resulting in a pulse model of the change in quasiparticle density within the trap as

$$\delta n_{\text{qp,trap}}(t) = \frac{N_{\text{qp}}^{r}}{V_{\text{tr}}}\frac{\tau_{\text{qp}}}{\tau_{\text{inj}} - \tau_{\text{qp}}}\left(e^{-t/\tau_{\text{inj}}} - e^{-t/\tau_{\text{qp}}}\right). \tag{4}$$

We will use this pulse model in Sec. IV C to numerically model the energy threshold resulting from a pulse reconstructed from a simulated parity signal.

To close, we stress that the only fundamental physical limits in the above energy collection process are on η_{pb} in both the absorber and trap, and timescales associated with bulk anharmonic down-conversion of phonons. All other efficiencies and time constants are in principle amenable to design optimization (for instance, by limiting the amount of inactive absorbing material) or to material science study (surface-promoted phonon down-conversion due to surface treatment). We summarize some of the quantities discussed in the previous sections in Table I and provide baseline values we use in the rest of the paper.

C. QPD energy and charge parity

The QPD Hamiltonian is described by the modified CPB Hamiltonian [82],

$$H_{\text{CPB}} = 4E_C\left(\hat{n} - n_g + \frac{P-1}{4}\right)^2 - E_J\cos\hat{\phi}, \tag{5}$$

TABLE I. Summary of efficiencies and estimated values, as described in Secs. III A and III B, and visualized in Fig. 4.

Efficiency	Estimate	Notes
$\boldsymbol{\eta_{ph}}$ [from Eq. (1)]	0.65	$f_{surf} = 0.04$ $N_{surf} \approx 10^3$ [57] $f_{abs} \approx 0.1$ [57] $f_{loss} \approx 0.35$ (see Sec. III A)
$\eta_{pb,abs}$ and $\eta_{pb,trap}$	0.5	Estimated from Refs. [60,61]
η_{ce}	0.32	$\eta_{ph}\eta_{pb}$
η_{tr}	0.4–0.7	Geometry dependent; see Appendixes B and C
$\Delta_{abs}/\Delta_{trap}$	4	For Hf/Al combo

where we have included the charge parity-dependent shift, $P = \pm 1$, to the offset charge n_g [83]. As is standard for a superconducting qubit, $\hat{n}$ and $\hat{\phi}$ are conjugate operators corresponding to the number of Cooper pairs on the island and the phase difference across the junction, respectively. $E_J = h\Delta/8R_N e^2$ is the Josephson energy, the barrier tunneling energy of Cooper pairs, with R_N the normal-state resistance of the junction. $E_C = e^2/2C_\Sigma$ is the charging energy interpretable as the energy required to shift the island charge by an electron. C_Σ is the total capacitance between the island and its circuit environment, formed from the sum of gate (C_g), junction (C_J), and shunt (C_s) capacitances (see Fig. 1). Following Ref. [83], a charge parity switch event, from $P = +1$ (even) to $P = -1$ (odd), shifts the offset charge by half of a Cooper pair and hence shifts the energy spectrum. We label the eigenstates of the CPB Hamiltonian by the state index $i = 0, 1, 2, \ldots$ and charge parity terms $p = e, o$.

We consider two limits of the CPB Hamiltonian, corresponding to both styles of QPD, which are distinguished by the dominant energy scale: $\xi = E_J/E_C$. For a CPB, the use of a small (few femtofarad) junction capacitance and the absence of shunt capacitance yield a large charging energy and $\xi \lesssim 1$. In the CPB limit, due to the curvature of the ground state, the difference between even and odd charge parity energy levels δE can be large and of the same order as E_J. For an OCS, a large $\mathcal{O}$(100 fF) shunt capacitor, added to flatten the energy levels in order to decrease sensitivity to environmental charge [35], results in a smaller charging energy and $\xi \gtrsim 1$. Note that only the lower energy levels are substantially flattened; the higher energy levels still exhibit a significant energy difference between even and odd states. As we operate the qubit in the ground state even in the OCS case, a frequency shift in the readout resonator is now the result of coupling to the even-odd energy difference of higher energy levels. Solutions to this Hamiltonian and respective even-odd energy spectra for a suggestive set of parameters are shown in Fig. 5.

D. Quasiparticle tunneling

For QPD operation, two characteristic tunneling rates are relevant: the rate for quasiparticles to tunnel into the island or pad, Γ_{in}, and the rate for quasiparticles to tunnel out of the island or pad, Γ_{out}. From symmetry considerations, assuming equal absorber sizes, an OCS QPD has $\Gamma_{in} = \Gamma_{out}$. Closed-form expressions can be calculated for Γ_{in} and Γ_{out} assuming that the density of nonequilibrium quasiparticles, δn_{qp}, is uniform throughout the absorber [24,84,85]. For typical device parameters, this approximation is justified since the quasiparticle diffusion timescale is much shorter than the quasiparticle tunneling or quasiparticle recombination timescales (see Appendix E). Under this assumption, one can define effective chemical potentials for the more general case of the CPB with absorber and island [22] of $\delta\mu_{abs,island}$ (see Appendix D for specifics).

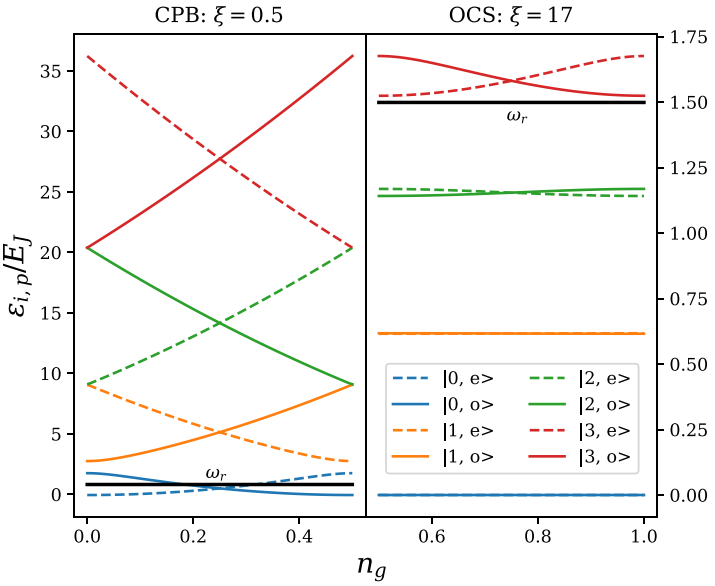


FIG. 5. Example energy level structure from solving the CPB Hamiltonian for CPB (left) and OCS (right) ξ ratios, with $E_J/2\pi \sim 5$ GHz. The placement of the readout resonator is given by the black line.

Using these effective chemical potentials, the rate for a thermalized quasiparticle to tunnel from the absorber to the island is given by Fermi's golden rule [22,25,85]:

$$\Gamma_{\text{in}} = \frac{16E_J}{h\Delta}\int_{\Delta}^{\infty} dE \frac{E(E+\delta E)-\Delta^2}{\sqrt{(E^2-\Delta^2)[(E+\delta E)^2-\Delta^2]}} f(E-\delta\mu_{\text{abs}})[1-f(E+\delta E-\delta\mu_{\text{island}})], \quad (6)$$

where $f(\epsilon)$ is the Fermi-Dirac distribution. The energy difference between odd and even parity for the ground state, δE, renders the island a potential well of depth δE (for the electron component of an absorber quasiparticle), effectively shifting the energy spectrum of the island states δE below that of the absorber. Because $k_B T, \delta E \ll \Delta$, the Fermi level is well below Δ and the $1 - f(\epsilon)$ factor does not block tunneling: Γ_{in} is determined entirely by the absorber quasiparticle density, even in an OCS.

It is important to note, however, that since we have $E_c \gg E_J$ in the CPB limit, we therefore have $\delta E \gg E_J$ [85]. Thus, when a quasiparticle has tunneled on to the island, the island energy spectrum shifts upward by δE *and* the lowest energy state for a quasiparticle on the island is occupied, blocking the tunneling of additional absorber quasiparticles [86] until the quasiparticle on the island tunnels out.

In an OCS, because $E_C \ll E_J$, there is no such blockade. Thus, any number of quasiparticles can tunnel back and forth between absorbers, and $\Gamma_{\text{in}} = \Gamma_{\text{out}}$.

For the OCS case, we can move away from the integral form for Γ_{in} and work with the linearized form for small n_{qp} (see Appendix D for derivation):

$$\Gamma_{\text{in}} \approx \frac{16E_J k_B T}{\mathcal{N}\Delta h} n_{\text{qp}} \equiv K n_{\text{qp}}. \quad (7)$$

Because the above form neglects δE, it is only approximately correct for the CPB case. Regardless, Γ_{in} is proportional to the quasiparticle density for both architectures. One can engineer the generic tunneling proportionality constant, K, by changing E_J, Δ, $\mathcal{N}$ (the quasiparticle density of states defined in Appendix D), or δE if applicable. Equation (7) is a key result of our work, providing for

a closed-form tunneling rate expression that can allow for both event reconstruction and detector optimization.

Γ_{out} is more complicated for a CPB because of the aforementioned shift of the energy spectrum after tunneling has occurred. The island quasiparticle now has the same energy as the gap energy of the absorber, the energy it had before tunneling [87]. Therefore, one must calculate the "elastic" tunneling rate, which is valid more generally when quasiparticles tunnel out after tunneling in without first relaxing to a lower energy. For a full discussion of the lead-to-island tunneling rate in the CPB case, see Ref. [22]. In Sec. IV C, we outline how the differences in the tunneling rate of OCS and CPB devices affect device performance and expected energy thresholds.

E. Readout details

As is typical, we read out the charge parity state of the QPD by capacitively coupling it to a superconducting resonator [25,83] in the dispersive limit [46]. There is extensive experience with this approach in the literature for charge parity state detection, particularly for QCDs [27,28]. The use of a readout resonator decouples the qubit design (E_J and E_C particularly) from the requirements on the readout—The qubit can be optimized for energy sensitivity, and then the readout resonator adapted to the qubit design. Furthermore, the very low readout powers ($\lessapprox -140$ dBm) required for direct qubit-to-feedline coupling, along with the potential for unwanted, readout-power-generated quasiparticles seen in other superconducting systems [32], make a coupled resonator an attractive readout method.

With a dispersive readout, the qubit is far detuned from the resonator, preventing direct exchange of energy between the two systems [46]. Instead, the state of the qubit shifts the resonant frequency of the readout resonator from its bare value by an amount $\chi_{i,p}(n_g)$ (for qubit state i and charge parity state p) that can be measured through a transmission measurement $S_{21}^{i,p}$.

The tunneling proportionality K from Sec. III D suggests that tunneling rates can approach for $\mathcal{O}(100)$ kHz for reasonable shifts in quasiparticle density. In order for the resonator to readout such a high tunnel rate with good fidelity, the readout resonator's signal bandwidth, f_r/Q_r, must be larger than the tunneling rate. A loaded quality factor of $\mathcal{O}(10^4)$ dominated by the coupling ($Q_r \approx Q_c$), in a $\mathcal{O}$(GHz) resonator, would meet said requirement by providing $\mathcal{O}$(MHz) signal bandwidth.

A key difference between CPB- and OCS-style QPDs is the mechanism responsible for the shift in resonator frequency. For CPBs, the existence of a strong relationship between gate charge and energy is interpretable as an effective quantum capacitance [25],

$$C_{i,p} = -\frac{C_g^2}{4e^2}\frac{\partial^2 \epsilon_{i,p}}{\partial n_g^2}. \tag{8}$$

The change in this charge-parity-state-dependent capacitance $C_{i,p}$ shifts the readout resonator frequency [25]. The shift can be approximated in the reduced two-state Hilbert space case as

$$C_{i=(0,1),p} \approx 4\frac{C_g^2}{\xi C_\Sigma} \rightarrow \chi_{i=(0,1),p} \approx -\frac{1}{2}\omega_r^3 L_r C_{i=(0,1),p}. \tag{9}$$

In the transmon regime ($\xi \gg 1$), Eq. (9) implies that the quantum capacitance vanishes. Instead, the shift in ω_r is dominated by an alternative shift [83]. This $\chi_{i,p}$ can be derived from the full CPB-resonator Hamiltonian (see Ref. [88]) using second-order perturbation theory,

$$\chi_{i,p} = g^2 \sum_{j\neq i} \frac{2\omega_{ij,p}|\langle j,\, p|\hat{n}|i,\, p\rangle|^2}{\omega_{ij,p}^2 - \omega_r^2}, \tag{10}$$

where $\omega_{ij,p}$ is the transition frequency between transmon states $|i,\, p\rangle$ and $|j,\, p\rangle$, and g is the coupling between the transmon and the resonator. As with the Lamb shift in atomic orbitals, photons in the readout resonator, even if not resonant with the qubit transitions, can be virtually absorbed and reemitted by the qubit, causing a shift in the energy of $|i,\, p\rangle$. Because of the denominator in

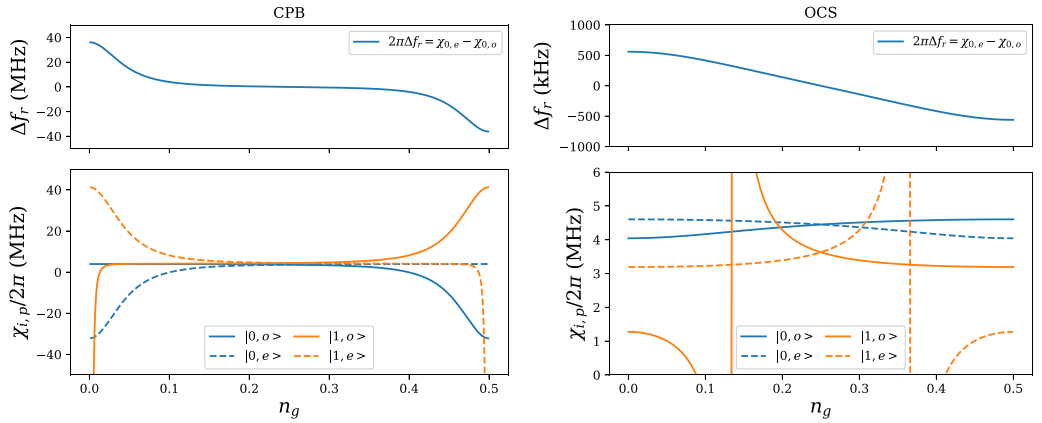


FIG. 6. Top: Absolute difference in resonator frequency between even and odd charge parity for the ground states of a CPB (left) and OCS (right). Bottom: Shift in resonator frequency of the ground and first excited states of a CPB due to the quantum capacitance shift (left) and an OCS due to the dispersive shift (right).

Eq. (10), the effect is larger the closer the photon is to a qubit transition, and so we engineer the largest possible shift by placing ω_r close to an energy level difference $\omega_{j,p} - \omega_{i,p}$. We choose to place ω_r close to ϵ_{03}, as also shown in the right panel of Fig. 5.

Assuming reasonable parameters for various components, we can see $\chi_{i,p}(n_g)$ for the CPB and OCS in Fig. 6, along with the absolute difference in resonant frequency $\Delta\omega_r^i = (\chi_{i,e} - \chi_{i,o})$. We see that for ground-state shifts, $\Delta\omega_r^{\max}/2\pi = \mathcal{O}(\text{MHz})$ for the CPB and $\Delta\omega_r^{\max}/2\pi = \mathcal{O}(100)$ kHz for the OCS. The CPB shift is of the same size as the FWHM and is eminently resolvable. While the OCS shift is smaller, the nominal frequency uncertainty of a thin-film superconducting resonator, read out at low power and limited by $4K$ amplifier noise, is $\mathcal{O}(100)$ Hz [49,50]. These shifts should be easily resolvable at expected operating powers ($\sim$−90 dBm at device) without special attention to readout strategy and crucially without requiring the use of any quantum-limited amplifier with subkelvin noise temperatures.

One complication in operating multiple QPDs on the same feedline (for use cases requiring pixelization) is that a gate bias value V_g will not match the optimal operating point for all sensors, due to inherent uncorrelated static charge drifts for each sensor. As Fig. 6 makes clear, one needs to operate at half-integer n_g values corresponding to peaks in the resonator response. A potential solution is to *sweep* the bias in a similar fashion to Ref. [27]. Briefly, by ramping the bias in a sawtooth manner at a frequency f_{ramp} as shown in Fig. 7 (top), one traces through an entire cycle of n_g for all sensors. In an OCS QPD, tunneling events will break the smooth variation in $\chi_{i,p}$ and this effective phase shift is now the signature of a single tunneling event. The caveat is that if the period of the ramp signal is significantly longer than the expected signal lifetime ($\sim 3\tau_{\text{qp}}$), a quasiparticle burst may occur as the sweep passes the point where $\delta E = 0$ between the even and odd states; hence, a large portion of the signal may be lost as Δf_r dips below the noise floor. This issue can be partially addressed by ensuring that the period of the ramp signal is less than half of the expected signal lifetime; in this case, you will only lose the fraction of signal roughly equal to the fraction of the periodic ramp where Δf_r dips below the noise floor ($<$10% with conservative estimates). This technique is more complicated for CPB QPDs, as the relative energy level of a quasiparticle on the island is higher for $n_g = (0, 2e, \ldots)$ [89] than in the absorber as the island depth δE flips sign with the changing n_g as seen in Fig. 3. At and near these points then, the small CPB island is effectively instantaneously cleared. This behavior does not manifest for an OCS device as δE is negligible with increasing ξ. Thus, in a CPB QPD, such a rapid gate sweep will preferentially keep the device in the even state. However, episodes of rapid tunneling, such as after a burst of produced quasiparticles, will suppress peaks in the trace and produce "gaps" of one to a few peak widths

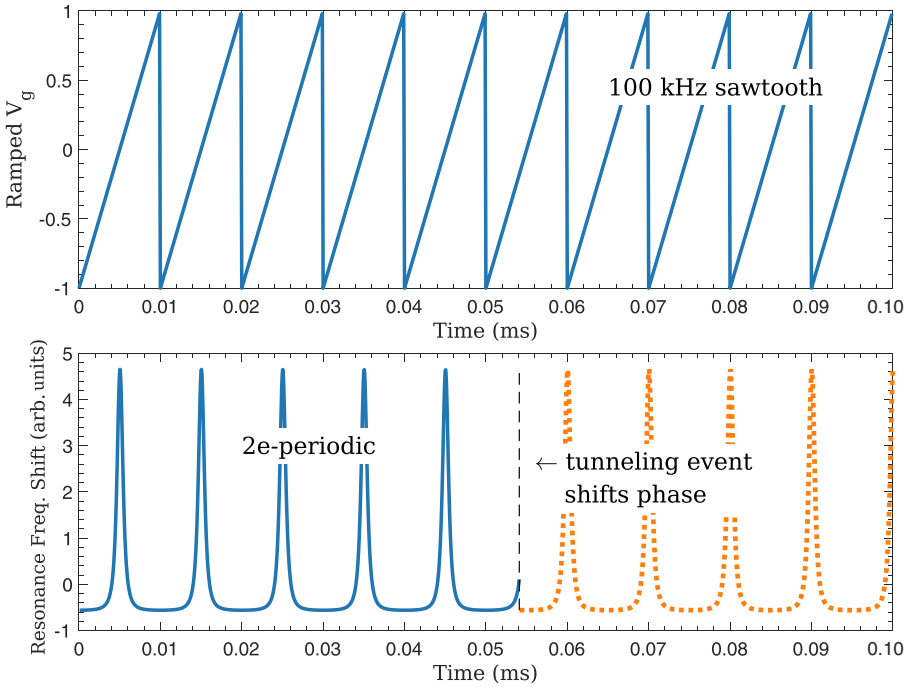


FIG. 7. Top: Example of a sawtooth voltage bias sweep at 100 kHz. Bottom: The stylized frequency shift expected when in the even state is given by the blue curve. A tunneling event in an OCS QPD effectively shifts the phase of this signal by shifting from the even → odd curves and introducing a noticeable gap in the output signal.

in $\chi_{i,p}$ [27] before the periodic trace resumes. While the number of tunneling events cannot be ascertained from the presence of a gap, it can be used to tag discrete energy deposits that generated the rapid tunneling—potentially from single-phonon absorption.

IV. DEVICE PERFORMANCE

Computing QPD performance, through modeling of expected signal and background rates, requires grappling with a variety of challenges—including the stochastic nature of the discrete charge parity transitions and asymmetric tunneling (at least in the case of the CPB), among other issues. To begin our discussion, we catalog expected fundamental and readout-related noise sources in Sec. IV A. Next, we investigate a simplified device model in Sec. IV B, considering only OCS QPDs to get a flavor of expected performance metrics. Here, we express our results in the more analytically tractable unit of number of transitions within a given period. Finally, Sec. IV C provides a more robust numerical modeling, using charge parity state dwell times instead and taking into account the effects of pulsing and asymmetric time-varying tunneling rates, and further discusses the factors that may affect our ability to disentangle signals from background.

For concreteness, we provide parameters for four hypothetical devices in Table II, investigating different trap material choices (aluminum [90] versus hafnium) and device styles. The Hf case reflects an optimistic, yet plausible, scenario regarding the use of a material with favorable properties and thermal backgrounds. To avoid the confounding effects of backgrounds (e.g., radiogenic, cosmogenic, or other otherwise unexplained excesses [91]), the choice of substrate, geometry-dependent phonon-to-film couplings, and quasiparticle diffusion, we only deal with absorbed energy E_{abs} bounds, which roughly reflects intrinsic sensor properties.

TABLE II. Basic operating characteristics for device examples discussed in text with example E_{abs}. Assuming thermal quasiparticles comprise the entirety of the quiescent background. Literature values of Hf thin-film quasiparticle lifetimes are ∼400 μs [92], though to our knowledge, and unlike Al, no serious R&D effort has been undertaken to extend this—which suggests significant improvement can be achieved in this frontier.

	Aluminum			Hafnium	
Style	CPB	OCS		CPB	OCS
V_{tr}	100 μm^3	50 μm^3 (×2)		1000 μm^3	500 μm^3 (×2)
T_c	1.2 K			0.25 K	
T_{opr}	0.1 K			0.025 K	
Δ	190 μeV			40 μeV	
E_{abs}	200 meV			40 meV	
n_0	0.3 μm^{-3}			0.03 μm^{-3}[a]	
E_J/h	4.9 GHz	6.14 GHz		4.9 GHz	6.14 GHz
E_C/h	11.1 GHz	356 MHz		11.1 GHz	356 MHz
ξ	0.5	17		0.5	17
Fano factor F			0.2		
τ_{qp}			1 ms[b]		
τ_{inj}			2 ms		
K	3 kHz μm^3			20 kHz μm^3	
Γ_{out}	2 kHz	n/a		10 kHz	n/a

A. Noise sources

To properly estimate the performance of a QPD, we list some expected contributions to the noise and how they will be modeled in the sections that follow.

Telegraph noise. A pulse in the quasiparticle tunneling-in rate results in a two-state time-dependent charge parity response in the QPD. This two-state flip-flop is referred to as a *telegraph* process. This telegraph noise represents noise *during* a pulse that may affect energy resolution at nonzero energy. For determining the threshold from the baseline (zero-energy) noise, we focus on the shot noise on the quiescent tunneling rates $\Gamma_{\text{in,out}}$, where the variance on the number of tunneling events in a given time period equals the expected mean number of tunneling events in that period.

Residual quasiparticle noise. For thin-film aluminum, a quiescent (residual or steady-state) quasiparticle density of $n_0 = 0.01$–1 μm^{-3} has been measured in qubit systems [51], with the population influenced by thermal or other pair-breaking processes [93]. We can account for the effect of this population by again modeling it as a super-Poissonian shot noise with variance proportional to the total quasiparticle number $\sigma^2 = 16 n_0 V$ (the prefactor comes from including pairing effects for phonon to quasiparticle breaking and recombination rates).

Fano noise. For a given phonon energy deposit, the same number of quasiparticles will not always be generated. The process is not, however, Poissonian because of correlations between the creation process for the quasiparticles. The sub-Poissonian nature is encoded in the Fano factor [94]. We include this contribution in our energy resolution modeling with $\sigma^2 = F N_{\text{qp}}^r$. As a first pass, we take F to be ≈0.2 [95], a number calculated for quasiparticle production from photon absorption $\gg 2\Delta$. Its application to low-energy phonon absorption will need to be experimentally validated.

System and amplifier noise. Amplifier noise can potentially limit the ability to observe charge parity transitions. The fractional noise on resonance due to amplifier noise is given by [12]

$$\frac{\delta f}{f_r} \approx \sqrt{\frac{k_B T_N \Gamma_{\max}}{2P_g}} \frac{Q_c}{Q_r^2}. \tag{11}$$

For conservative assumptions of noise temperature $T_N = 10$ K, feedline (readout) power of $P_g = -120$ dBm, coupling quality factor $Q_c = 10^4$ ($\approx$ the loaded value Q_r), and a resonator bandwidth set in concordance with the maximum expected tunneling rate $\Gamma_{\max}$ of 1 MHz (corresponding to the expected transition rate given a 10 eV energy deposition directly into an OCS device absorber), the fractional frequency noise is 70 kHz. This is $\ll \Delta f_r$ from Sec. III E (even for the smaller shifts seen by the OCS style QPD).

TLS noise. Two-level system (TLS) noise is often significant for thin-film superconducting resonators [50,77]. TLS has also been seen to limit qubit coherence lifetimes [96]. We can calculate the impact of TLS noise in the same way as for amplifier noise: We integrate a typical TLS noise power spectral density (PSD) [77,97], $S_{\delta f/f}$, over a similar bandwidth $\Gamma_{\max}$ as for amplifier noise and find

$$f_r \sqrt{\mathcal{S}_{\delta f/f} \Gamma_{\max}} \sim 10\,\text{kHz}. \tag{12}$$

As in the case of amplifier noise, the rms noise is much smaller than the charge parity transition signal and so does not factor into sensitivity.

B. Performance estimates

We are now in a position to provide estimates for QPD performance. For a given time window $t_w = t_f - t_0$, the expected number of transitions S_w can be computed as an inhomogeneous Poisson process by integrating the expected pulse shape,

$$S_w = \int_{t_0}^{t_f} K \delta n_{\text{qp}}(t) dt. \tag{13}$$

For our pulse model from Eq. (4), the total expected number of transitions from the entire pulse (with $t_w \gg \tau_{\text{inj,qp}}$) is

$$S_{\text{avg}} = \frac{K}{V_{\text{tr}}} N^r_{\text{qp}} \tau_{\text{qp}}. \tag{14}$$

We note the straightforward dependence on increasing the signal transitions, by increasing the tunneling proportionality (for instance, by increasing E_J), decreasing the trap volume V_{tr}, and increasing τ_{qp}.

A simple expression for the stochastic background can be obtained by defining the random variables:

$$\begin{aligned} \boldsymbol{N_0} &\sim \text{Gaussian}(N_0, \sigma = 4\sqrt{N_0}), \\ \boldsymbol{B} &\sim \text{Poisson}\left(B_{\text{avg}} = \frac{K t_w}{V_{\text{tr}}} \boldsymbol{N_0}\right), \end{aligned} \tag{15}$$

with N_0 the quiescent quasiparticle population (in quasiparticle number units) and $\boldsymbol{B}$ the background number of transitions within the window, taking into account the telegraph shot noise. Note that $\boldsymbol{B}$ is a mixture distribution. In the limit of a large number of transitions, we can treat $\boldsymbol{B}$ as a Gaussian process, which allows us to write the variance in the background distribution as the distributed

TABLE III. Expected signal and background transition counts and resolvable absorbed energy threshold for OCS-style devices, using the example parameters provided in Table II, for a window $t_w = 3\tau_{\rm abs}$.

	Aluminum	Hafnium
$S_{\rm avg}$	20	13
$B_{\rm avg} \equiv \langle \boldsymbol{B} \rangle$	3.6	2.4
$\sigma_{B_{\rm tot}}$	2.0	1.6
σ_S	8.9	7.1
$E_{\rm abs}$ threshold (meV)	165	37

product,

$$\sigma_{B_{\rm tot}}^2 = \sigma_{N_0}^2 \left(\frac{dB}{dN_0}\right)^2 + \sigma_B^2 = \left(K t_w + 16 \frac{K^2 t_w^2}{V_{\rm tr}}\right) n_0. \tag{16}$$

The signal variance can be written in a similar way, including the telegraph and Fano components, as

$$\boldsymbol{N_F} \sim \text{Gaussian}\left(N_{\rm qp}^r, \sigma_{\rm F} = \sqrt{F N_{\rm qp}^r}\right), \quad \boldsymbol{S} \sim \text{Poisson}\left(\frac{K \tau_{\rm qp}}{V_{\rm tr}} \boldsymbol{N_F}\right). \tag{17}$$

As we are interested in a sensitivity estimate here, we elide the changing transition rate due to the varying pulse shape and use only the overall number of transitions from Eq. (14). Treating $\boldsymbol{S}$ as Gaussian for tractability, we have

$$\sigma_S^2 = \left(K \frac{\tau_{\rm qp}}{V_{\rm tr}} + K^2 \left(\frac{\tau_{\rm qp}}{V_{\rm tr}}\right)^2 F\right) N_{\rm qp}^r. \tag{18}$$

Inputting the parameters from Table II into Eqs. (14)–(16) and (18), we arrive at the values in Table III. We have used Eq. (14) to convert σ_B into a "5σ" threshold, the minimum energy deposit potentially resolvable from background. The values, particularly for the larger Hf device and extrapolating downward in volume, reflect the potential to resolve single-phonon events.

The crucial point, we stress, is that it is the volume of the trap and *not* the absorber that sets the tunneling rate. Referring to Appendix B, we note that the fraction of quasiparticles tunneling into the trap $\eta_{\rm tr}$ can be engineered to be $\approx$0.2. Such a regime yields $N_{\rm trap} \approx \mathcal{O}(0.1\text{–}1) \times N_{\rm abs}$, as the quasiparticle multiplication effects offset the trapping fraction. Thus, the number of quasiparticles produced in the much smaller Hf trap can be similar to that within the Al absorber.

Care needs to be taken to account for the quiescent quasiparticle density in the absorber and its effect on the quasiparticle density in the trap. Nonthermal mobile background quasiparticles created in the absorber, such as through a constant source of background IR radiation [81], may impact the density in the trap because the trap acts as a sink. We can estimate the size of this effect using a simple balance model (see Appendix F) that factors in generation, recombination, and trapping. For a seemingly negligible excess density of $n_0 = 0.05\ \mu\text{m}^{-3}$ in reasonably sized Al absorber pads of $\sim$60 000 μm^3 total (2 $\times$ 400 μm $\times$ 200 μm $\times$ 600 nm), a 500 μm^3 Hf trap would have a much higher (than purely thermal origin) quasiparticle density of $n_0^{\rm trap} \sim 0.15\ \mu\text{m}^{-3}$. By propagating expected trapping and phonon efficiencies (as detailed in Appendix C), we find for this system a resolution and threshold of energy *deposited in the substrate* of $\sigma_{\rm dep} \approx 100$ meV (i.e., $E_{\rm dep}^{\rm threshold} \approx 500$ meV).

It will be crucial then to drive down n_0 in the absorber to the thermal floor. In such a condition, the dominant background will again be the thermal density within the trap alone. Appendix C computes the resolution on deposited energy for a 1 cm^2 crystal and 50 QPDs (for 4% area coverage), resulting in

$$\sigma_{\rm dep} \approx 70\left(\frac{V_{\rm trap}}{800\,\mu{\rm m}^3}\right)^{\frac{1}{2}}\ {\rm meV}. \tag{19}$$

Such a design would immediately allow for the sensing of single optical phonons. Optimization of the trap volume down to tens of μm^3 with corresponding developments in quasiparticle trapping into junction materials (e.g., hafnium) would result in a threshold of just a few tens of meV, with the ability to probe for signals from the bulk distribution of acoustic phonons. All told, these calculations demonstrate the potential to *detect* and *reconstruct* $\ll$eV substrate energy deposits, providing a path to sensitivities beyond currently demonstrated technologies [10,12].

C. Energy reconstruction and thresholds

Having covered a basic model of the signal and noise, we are ready to work through more concrete, numerically simulated performance metrics. We simulate the two-state, charge parity signal of a QPD in response to an energy deposit, folding in the fundamental noise sources discussed in the previous section. We consider the case of a device consisting of a single superconducting material and discuss sensitivity on $E_{\rm abs}$, restricting ourselves once again to only the intrinsic sensor physics. These results can heuristically be extended to $E_{\rm dep}$ by factoring in the various collection efficiencies (i.e., $\eta_{\rm ce}$ and $\eta_{\rm pb}$) by hand.

We start by discretizing pulses [defined by Eq. (4)] and their time spans into bins of width t_w, using values from Table II in their construction. Next, for each time bin, we sample a Poisson distribution to determine whether charge parity state transitions occur in the given interval. In any experimental realization, the sampling frequency must also be chosen to ensure that the probability of more than one transition occurring in a window is negligible. The relevant Poisson parameter depends on both the current charge parity state and whether the device is a CPB or OCS:

$$\lambda_{\rm even} = S_w(\mathbf{N_F}) + B_{\rm avg},$$
$$\lambda_{\rm odd} = \begin{cases} \lambda_{\rm even}, & \text{OCS}, \\ \Gamma_{\rm out} t_w = \text{constant}, & \text{CPB}, \end{cases}$$

where $S_w(\mathbf{N_F})$ should be interpreted as initially sampling $\mathbf{N_F}$ from Eq. (17), taking that number to be $N^r_{\rm qp}$ in Eq. (4), and subsequently computing S_w from Eq. (13). From this process, we can construct a telegraph signal time series of transitions, an example of which is shown by the blue curve in Fig. 8. To reconstruct a pulse, we first convert its telegraph signal to a series of even and odd state dwell times, $\delta t_{e,o}$, defined as how long the system stayed at its last charge parity until a transition occurred. We then estimate the Poisson parameter at each bin a transition occurs, as

$$\hat{\lambda}_{\rm even,odd} = \frac{t_w}{\delta t_{e,o}}.$$

This prescription provides us with a series of points in time that are samples of the true transition rate, seen as the orange points in Fig. 8. We can fit these data with a two-parameter model ($\delta n_{\rm qp}$, n_0) incorporating the expected pulse shape and quiescent quasiparticle density, with results shown as the orange best-fit line in the figure. For this simulation, we assume that we know the pulse start time, while a more complete simulation would fit it as a free parameter (and accept the corresponding impact on threshold).

There are a few subtleties that depend on the value of ξ. Because tunneling in is blocked when the CPB is in the odd state, the total number of observed qubit state transitions in any interval will be a factor of roughly $2\Gamma_{\rm out}/(\Gamma_{\rm in} + \Gamma_{\rm out})$ fewer in the CPB case (for equivalent $\Gamma_{\rm in}$). Furthermore,

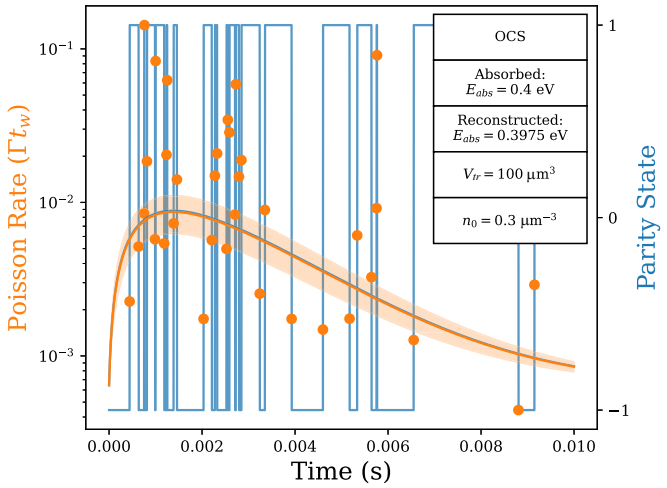


FIG. 8. Simulated charge parity state time series (blue telegraph signal) for parameters given in inset. Dwell time points derived from this trace, converted to an equivalent transition rate, are given as the orange circles. The pulse reconstruction is shown by the orange line, with the shaded band corresponding to 1σ on the reconstructed energy.

since the OCS tunneling is bidirectional, both even and odd dwell times provide information about the quasiparticle density, whereas in the CPB only, Γ_{in} is proportional to quasiparticle density.

For each of the device parameter cases provided in Table II, we repeat this simulation thousands of times to characterize the energy threshold and reconstruction, shown in Fig. 9. The shaded bands reflect the 1σ deviation in reconstruction. For regions where the distribution of reconstructed events is non-normal, such as at zero to low energies, we instead compute 1σ equivalent quantiles. We infer "5σ" thresholds from the baseline resolution reconstructed from simulations with no energy deposit.

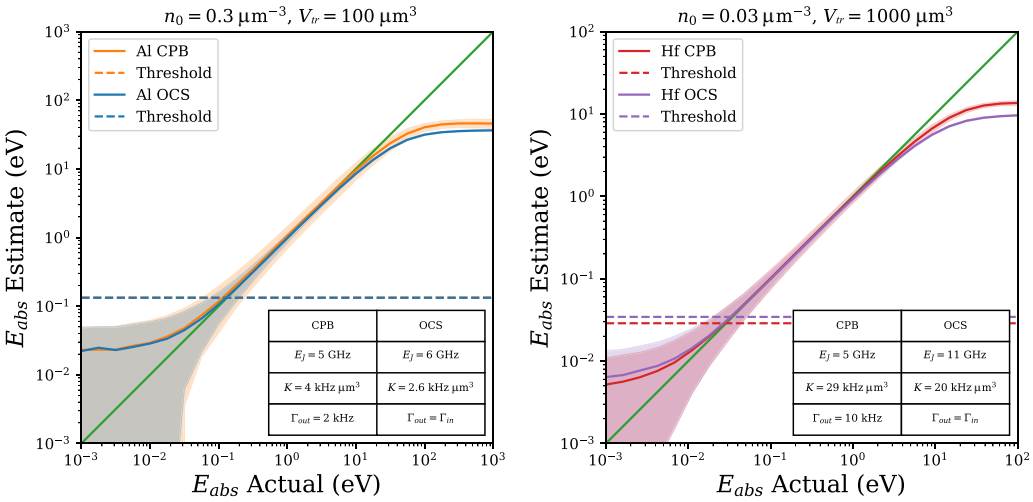


FIG. 9. Left: Reconstructed energy estimate vs simulated energy absorbed by single aluminum CPB and OCS sensors with 100 μm^3 trap volume. Right: Similar curves for Hf devices with 1000 μm^3 total volume of absorber. 1σ equivalent quantiles are given by the shaded bands, with energy thresholds (described in text) shown as the dotted lines.

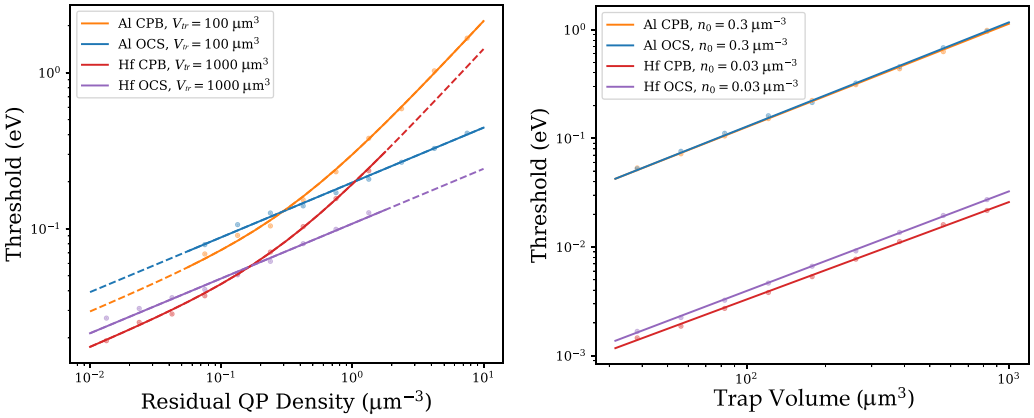


FIG. 10. Left: Simulated effect of quiescent quasiparticle density on E_{abs} threshold. n_0 is simulated in the neighborhood of Table II values and extrapolated based on expected behavior elsewhere. Right: Simulated effect of volume on E_{abs} threshold.

We note the consistency between these thresholds and the approximate values from Sec. IV B. For sufficiently low E_{abs}, the residual quasiparticle density n_0 sets the threshold. At high E_{abs}, saturation occurs in both sensor modalities when the tunneling rate exceeds the resonator bandwidth, $\Gamma_{in} > Q_r/\tau_r\pi$, and one cannot accurately reconstruct the number of transitions due to the slow resonator response. This result implies that the resonator should be designed to accommodate the typical tunneling rate, perhaps at a cost in Q_r and thus in signal-to-noise ratio for the charge parity transition relative to amplifier noise.

While the OCS and CPB schemes have comparable thresholds (almost identical for the Al device due to judiciously chosen parameters), they differ in other performance metrics. The CPB suffers larger reconstruction variance (note the size of the bands in Fig. 9) because the constant nature of Γ_{out} results in fewer transitions for a given energy deposit. Also, the CPB threshold degrades more dramatically with increasing n_0, as seen in Fig. 10 (left), than the OCS due to blocking of tunneling in. The two architectures' performance is only similar when $\Gamma_{in} \ll \Gamma_{out}$. It should be noted that, at high enough n_0, both modalities experience a degradation in sensitivity due to saturation, with the OCS saturating faster because of the higher number of transition per interval. The overall dependence on volume, as seen in Fig. 10 (right), is as expected: A smaller volume provides a higher signal quasiparticle density for a given energy deposit, though this calculation neglects any potential related reduction in phonon collection efficiency. Also as expected, Hf offers lower threshold at the same n_0 than Al because of the higher quasiparticle yield per unit energy deposit. However, an increase in n_0 with decreasing Δ could counter this gain. Both QPD schemes have attractive features and deserve exploration for phonon sensing.

D. Additional considerations

In the preceding sections, we demonstrated that, for a reasonable set of assumptions and parameters, the QPD offers potentially groundbreaking energy threshold for phonon-mediated particle detection. A development program would begin with single-material devices to establish basic experimental parameters, followed likely by two-material devices incorporating quasiparticle trapping. Many choices must be made and challenges overcome, however, which we delineate here:

Material selection. There are a plethora of low-T_C (<1 K) superconducting materials, including alloys, that are suitable for thin-film applications—including W, AlMn, Ir, IrPt, Os, and Ti [98,99]. Workable tunnel junctions have not been convincingly demonstrated with most of these materials. Quasiparticle lifetime, phonon acoustic mismatch and collection, and amenability to device fab-

rication have not been exhaustively investigated. R&D on these and other lower-gap materials is warranted given the potential gain in responsivity.

Volume and diffusion. We have already discussed the effects of absorber/trap sizing and volume on tunneling rates in Sec. IV. However, the discussion there uses the shorthand of chemical potentials—convincingly used in the original QCD detector papers to demonstrate the linearity of the tunneling rate—while a more complete modeling would take into account the dynamic quasiparticle drift and diffusion processes. Those topics are, however, fraught with uncertainty, as briefly discussed in Appendix E, with varying literature reported values for diffusion coefficients and its dependence on temperature, film thickness, and gap [54,100–103]. Experimental verification, through direct measurement of QPD response, will prove crucial for determining future optimizations of absorber shape and sizing.

Quasiparticle cascade and trap design. As exhaustively studied in the cryogenic dark matter search (CDMS) experimental program (e.g., see Refs. [53,55,104] for theses spanning two decades), efficiently collecting quasiparticles within a constrained region, in absorber $\rightarrow$ trap designs, will be of paramount importance in maximizing phonon sensitivity. As is partially discussed in Appendix B, choices of absorber and trap lengths, material thicknesses, and overlap fractions will have to be simulated and tuned to achieve meV-scale E_{dep} thresholds. It is also imperative that n_0 be sufficiently low in the absorber, otherwise the absorber may significantly elevate the trap background level.

Vortices and quasiparticle trapping. Reference [105] discusses the impact of pinned (trapped) magnetic vortices, areas of quantized flux circulation. The local gap in these regions is driven to 0, and this sinklike behavior traps quasiparticles. Thus, pinned vortices in the QPD absorber could prevent quasiparticles from reaching the junctions. Reference [105] notices the geometrical dependence on pad shape for the vortex contribution, suggesting that this might be one avenue to reduce their importance. Furthermore, very high magnetic permeability shielding could be used to prevent vortices from forming in the first place [106].

Phonon loss simulations. Any phonon losses directly degrade the energy resolution of the QPD. As discussed in Sec. III A, literature values for η_{ph} vary widely between different experiments, making accurate determination of this parameter of vital importance. One promising avenue for accurate modeling is through use of bespoke phonon simulation software like G4CMP [107], with recent examples of phonon absorption simulations having been conducted for kinetic inductance detectors [108] and qubits [29]. Experimental techniques to reduce phonon loss could include suspending the substrate via hanging wirebonds [109] or in flip-chip designs where the ground plane and readout scheme are physically decoupled from the substrate [110,111].

V. APPLICATION TO A RARE-EVENT SEARCH AND CONCLUSION

To get a flavor of the science reach of QPDs, and with the performance curves of Sec. IV C in mind, we can consider their ability to probe for a light dark matter particle (mass m_χ) elastically scattering off a much heavier target (i.e., a silicon atom with mass m_T) [3]. From basic kinematics, the maximum energy transfer in such a two-body collision, if $m_T \gg m_\chi$, is $E_{\mathrm{max}} \approx 2m_\chi^2 v_\chi^2/m_T$. The dark matter velocity v_χ is constrained to be the Milky Way escape velocity of $\sim$600 km/s. Assuming all of E_{max} makes its way into the absorber (factoring in $\eta_{\mathrm{ph}} \sim 30\%$), a mixed Al/Hf device with a 75 meV deposit threshold, and no unexplained limiting background akin to a low-energy excess [91], could probe down to $m_\chi \sim 10\ \mathrm{MeV}\,c^{-2}$. Current experimental constraints for such elastically scattering light dark matter become weak at $m_\chi \sim 30$–$100\ \mathrm{MeV}\,c^{-2}$ [58,112,113]. Thus, QPDs could provide close to an order-of-magnitude improvement in probing light dark matter parameter space.

In summary, we have outlined a scheme of using qubit-derived sensors for rare-event search particle physics applications, leveraging a rich literature of devices constructed for quantum information purposes. We have described the relevant physics and operating principles for these resonator-coupled quantum parity detectors along with preliminary calculations for potential noise sources and detector sensitivity. We have argued that such devices are intrinsically able to detect tens

of meV energy deposits and, given further R&D into substrate-device couplings, should eventually be able sense single substrate-phonon events of a similar magnitude. QPDs could therefore be an excellent match to the challenge of detecting the lightest fermionic dark matter candidates. Ongoing fabrication efforts, based on designs presented in this paper, will hopefully experimentally verify the validity of the proposed schemes and calculations presented.

ACKNOWLEDGMENTS

We thank SLAC and FNAL collaborators for insightful conversations regarding qubits, phonons, and quasiparticles. This research was primarily supported by National Science Foundation PHY Grant No. 2209581 and the Schwartz/Reisman Collaborative Science Program between Caltech and the Weizmann Institute of Science. This work was also supported in part by the Defense Advanced Research Projects Agency (DARPA) under the Quantum Sensing of Neutrinos program (QuSeN). K.R. was supported in part by a Caltech Prize Postdoctoral Fellowship and J.E.P. by the Caltech SURF Program. This work was conducted at Washington University in St. Louis, California Institute of Technology, NASA's Jet Propulsion Laboratory, and the Weizmann Institute of Science.

DATA AVAILABILITY

Data and code are available upon reasonable request from the authors.

APPENDIX A: PULSE DYNAMICS

Quasiparticle pulse dynamics in our thin-film trap is described by the generation-recombination equation [114], specialized to the case of injection of energy $P(t)$:

$$\frac{dn_{\rm qp}}{dt} = \eta_{\rm ce}\eta_{\rm tr}\eta_{\rm pb,tr}\frac{P(t)}{V_{\rm tr}\Delta_{\rm tr}} - \frac{n_{\rm qp}}{\tau_{\rm qp}(n_{\rm qp})}, \tag{A1}$$

where, in general, the lifetime in the second term is

$$\tau_{\rm qp}(n_{\rm qp}) = \frac{1}{2Rn_{\rm qp}}, \tag{A2}$$

where the recombination constant R is material dependent. We assume that the injected power can be modeled as a simple exponential described by a single timescale:

$$\eta_{\rm ce}P(t) = \frac{E_{\rm abs}}{\tau_{\rm inj}}e^{-t/\tau_{\rm inj}}, \tag{A3}$$

$$\tau_{\rm inj} \approx \max(\tau_{\rm abs}, \tau_{\rm qp,abs}, \tau_{\rm tr}) \tag{A4}$$

for, as mentioned in Sec. III, an injection timescale set by a combination of a phonon absorption timescale, a quasiparticle lifetime in the absorber, and a trapping timescale, respectively.

The generation-recombination equation can be Taylor expanded for small a deviation $\delta n_{\rm qp}$ from the background quasiparticle density n_0, allowing one to assume a fixed $\tau_{\rm qp}$. That case, combined with our Eq. (A3) model of $P(t)$, yields the solution given by Eq. (4).

While this solution is not strictly valid for the case we consider here, $n_0 \ll \delta n_{\rm qp} = N^r_{\rm qp}/V$, we use this simple form with typical values of $\tau_{\rm qp}$ in order to capture the key elements of the dynamics. We believe these approximations are acceptable for this exploratory investigation while acknowledging that more precise modeling will be required for comparison to experimental demonstration data.

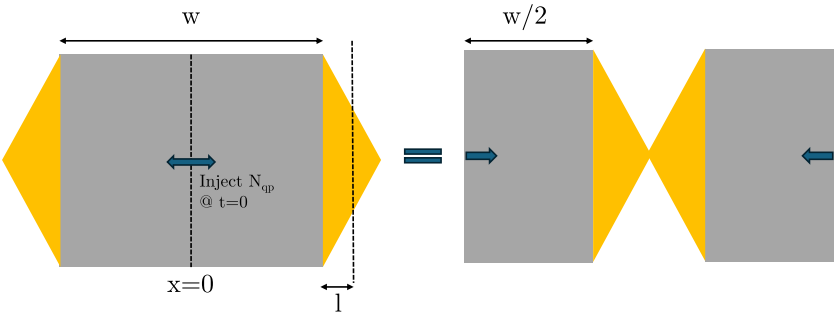


FIG. 11. Left: Sketch of a 1D diffusion model with N quasiparticles injected in an absorber (gray) with length scale w and trapped within a lower-gap region (gold) of length scale l. Nontrap boundaries are modeled as reflective. Right: This is equivalent to a transmon geometry. Sketch not to scale.

APPENDIX B: DIFFUSION AND TRAPPING FROM ABSORBER TO LEADS

We use the 1D analytic model of Angloher *et al.* [72], which describes the simplified geometry of Fig. 11, to estimate and confirm the applicability of a trapping architecture for quasiparticles generated within a large absorber and funneled to a lower-gap lead.

The fraction of trapped quasiparticles, $\eta_{\rm tr}$, given the geometry and labeled parameters of the figure, is

$$\eta_{\rm tr} = 2\frac{\sinh\left(\frac{\alpha}{2}\right) + \beta\cosh\left(\frac{\alpha}{2}\right)}{(1+\beta^2)\sinh(\alpha) + 2\beta\cosh(\alpha)} \tag{B1}$$

for $\alpha = w/l_d$, where l_d is a characteristic diffusion length dependent on absorber parameters (like film thickness). β reflects a trapping probability, estimated in Ref. [72] as $\beta = \tau_{\rm tr}/\tau_{\rm qp}$, for a quasiparticle trapping time and lifetime, respectively. We modify this prescription, given our much smaller trap, as $\beta = \tau_s/\tau_{\rm dwell}$ for a quasiparticle scattering time (thereby losing energy below the absorber gap) and a characteristic dwell time within the trap. This parametrizes the absorption probability across the boundary, allowing for quasiparticles to effectively be reflected back into the absorber.

We use $l_d = 300$ μm, an experimentally measured value for an Al absorber of thickness 500 nm [100]. $\tau_s \approx 0.2$ μs is computed using the formalism of Ref. [52]. The dwell time is estimated as $\tau_{\rm dwell} \sim l^2/D_{\rm trap}$, with trap length scale l and trap diffusion constant $D_{\rm trap} \sim 2\ {\rm cm}^2\ {\rm s}^{-1}$, which has been scaled for a thinner 100 nm trap thickness [100]. A resultant plot for the trapped quasiparticle fraction, for various trap lengths, is shown in Fig. 12. We see that reasonable $\mathcal{O}(0.1)$ values, in line with literature values [73,101], are achievable and can be plugged into our Eq. (C1).

The trapping efficiency depends on the quasiparticle transmission probability into the trap and a trapping timescale $\tau_{\rm tr}$ (the inverse of the rate at which a quasiparticle at $\Delta_{\rm abs}$ loses enough energy to be trapped, typically by phonon emission). Generally, only $\eta_{\rm tr}$ is experimentally measurable. For simplicity, we assume $\tau_{\rm tr} \ll \tau_{\rm inj}$, so it does not also need to be incorporated into Eq. (4).

APPENDIX C: ENERGY RESOLUTION OF A SENSOR ACHIEVING MAXIMAL PHONON COVERAGE

As an anchor, we use the sensor absorbed energy resolution of $\sigma_{\rm ref} = 6$ meV as per Fig. 9 (right) for a Hafnium trap and junction of $V_{\rm ref} = 1000\ \mu{\rm m}^3$. We envision a 1 cm^2 substrate, with 500 nm absorber films for phonon collection achieving 4% surface coverage, as detailed in Sec. III A, resulting in some number $N_{\rm sens}$ of sensors required to fulfill the constraints of Eq. (1).

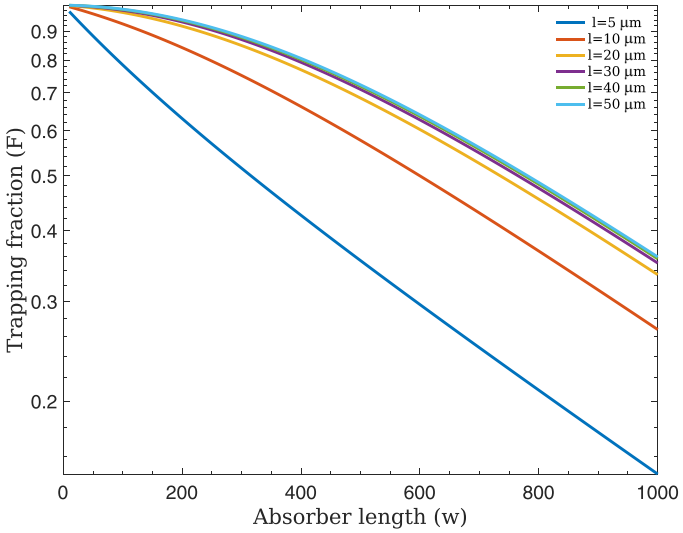


FIG. 12. Fraction of trapped quasiparticles as computed from Eq. (B1).

We use the formalism of Appendix B combined with our trapping relations of Sec. III A, to ascertain that the resolution on energy deposited within the substrate will scale as

$$\sigma_{\rm dep} = \frac{\sigma_{\rm ref}}{\eta_{\rm tr}\eta_{\rm pb,tr}\eta_{\rm ce}} \times \frac{\Delta_{\rm trap}}{\Delta_{\rm abs}} \times \left(\frac{V_{\rm trap}}{V_{\rm ref}}\right)^{1/2} \sqrt{N_{\rm sens}}. \tag{C1}$$

The results, plotted in Fig. 13, support the conclusions of Sec. IV B. A more detailed 2D simulation, combining measured diffusion/absorption parameters in both trap and junction *and* crucially factoring in the quiescent population n_0, will be required to determine an optimal geometry.

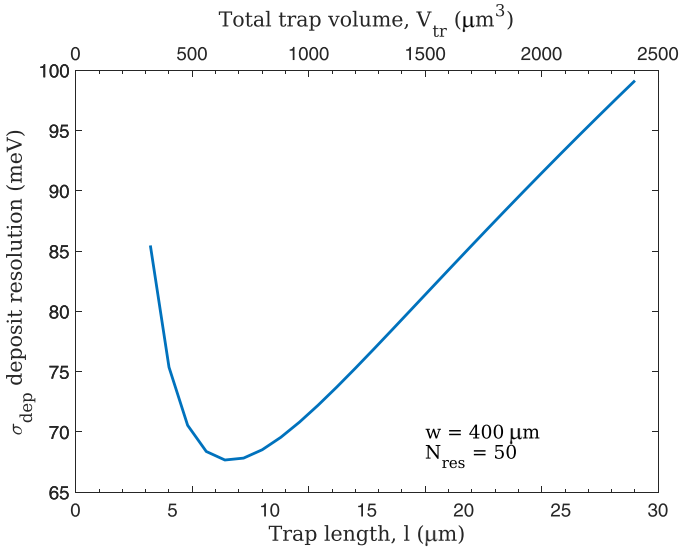


FIG. 13. Expected resolution on energy deposited within the substrate, factoring in expected trapping and phonon efficiencies.

APPENDIX D: TUNNELING RATE

We first reproduce a derivation for the chemical potential shift (as found in Ref. [22]) that sources the diffusion pressure for the quasiparticle tunneling. Following Ref. [115] closely in this section, we start by noting that the total quasiparticle density in a volume will be a sum of the nonequilibrium and residual populations and can be given by

$$n_{\rm qp} + n_0 = 2\int_{\Delta}^{\infty} D_f \frac{\epsilon^2}{\sqrt{\epsilon^2 - \Delta^2}} f_{\rm ne}(\epsilon) d\epsilon, \tag{D1}$$

where $D_f = 3\eta/2\epsilon_F$ is the normal metal density of states (η is the conduction band electron density and ϵ_F is the Fermi energy). The fractional term is the BCS density-of-states term for a superconductor. The factor of 2 accounts for holelike and electronlike states. If there are only a small number of quasiparticles and the volume is in thermodynamic equilibrium, then the quasiparticle distribution is nominally given by the Fermi function

$$f(\epsilon) = \frac{1}{1 + e^{\epsilon/k_B T}}$$
$$\epsilon = \sqrt{\left(\frac{\hbar^2 k^2}{2m} - \mu\right)^2 + \Delta^2}, \tag{D2}$$

with ϵ denoting the energy of a quasiparticle excitation with wave vector k in a superconducting volume. However, while the nonequilibrium quasiparticle population likely thermalizes rapidly ($\ll\mu$s) to equilibrium temperature T, it is *not* in chemical equilibrium. Thus, the chemical potential is shifted by $\delta\mu$ and the nonequilibrium quasiparticle distribution can instead be modeled by the Owen-Scalapino [116] form

$$f_{\rm ne}(\epsilon) = \frac{1}{1 + e^{(\epsilon - \delta\mu)/k_B T}}. \tag{D3}$$

Reference [115] solves for the expression of the chemical potential shift in terms of the nonequilibrium quasiparticle density by reexpressing Eq. (D1) through

$$n_{\rm qp} = 2D_f \int_{\Delta}^{\infty} \frac{\epsilon^2}{\sqrt{\epsilon^2 - \Delta^2}} (f_{\rm ne}(\epsilon) - f(\epsilon)) d\epsilon, \tag{D4}$$

which, to lowest order in $k_B T/\Delta$, results in

$$\delta\mu \approx k_B T \ln\left[1 + \frac{n_{\rm qp}}{\mathcal{N}} e^{\Delta/k_B T}\right], \tag{D5}$$

where $\mathcal{N} = D_f\sqrt{2\pi\,\Delta k_B T}$ is the density of available quasiparticle states. At low temperatures such that $n_{\rm qp} e^{\Delta/k_B T} \gg \mathcal{N}$, per Ref. [22], the above expression reduces to

$$\delta\mu \approx \Delta + k_B T \ln\left[\frac{n_{\rm qp}}{\mathcal{N}}\right]. \tag{D6}$$

In the case of asymmetric absorber and island, the terms in Eq. (D6) are indexed by their respective locations. Otherwise, they are equal for both pads.

We base our calculation of tunneling rates on Refs. [23,24,83,117], particularly the former two. The quasiparticle tunneling Hamiltonian is

$$H_T = \tilde{t} \sum_{l,r,s} \left[(u_r u_l - v_r v_l)\cos\frac{\hat{\varphi}}{2} + i(u_r u_l + v_r v_l)\sin\frac{\hat{\varphi}}{2}\right] \gamma_{r,s}^{\dagger} \gamma_{l,s} + \text{H.c.}, \tag{D7}$$

where $\tilde{t}$ is a tunneling matrix element, $\hat{\varphi}$ is the phase operator, (u, v) are electron and hole occupation factors indexed by the left (l) and right (r) electrodes of the tunnel junction, and γ are fermionic

annihilation/creation operators (s indexing spin). The tunneling (charge parity transition) rate from state i to j can then be computed from Eq. (D7) using Fermi's golden rule. As worked out in Ref. [24], this yields

$$\Gamma_{ij} = \frac{16E_J}{\pi\hbar}\left(|\langle j|\cos\frac{\hat{\varphi}}{2}|i\rangle|^2 S_{ij}^{-} + |\langle j|\sin\frac{\hat{\varphi}}{2}|i\rangle|^2 S_{ij}^{+}\right), \tag{D8}$$

where, in the low-energy regime, the tunneling rate has been factorized into two components: The matrix elements account for qubit state transitions, while $S_{ij}^{\pm}$ are "spectral functions" that handle initial state occupancy and final state blocking. In this detector concept, we do not rely on state changes and hence primarily work only with the ground state ($i = 0$, $j = 0$, $\delta\varepsilon_{ij} \sim 0$). Further, the electrodes are equivalent ($\epsilon_{l,r} \to \epsilon$) with equal chemical potential shifts. The only relevant spectral function is given by

$$S_{00}^{\pm} = \frac{1}{\Delta}\int_{\Delta}^{\infty} d\epsilon f_{\rm ne}(\epsilon)[1 - f_{\rm ne}(\epsilon)]\frac{\epsilon^2}{\epsilon^2 - \Delta^2}\left(1 \pm \frac{\Delta^2}{\epsilon^2}\right). \tag{D9}$$

For the transmon case, where $\chi = E_C/E_J \ll 1$, the cos and sin terms are shown in Ref. [23] to reduce to

$$\begin{aligned}
|\langle 0, p|\cos\frac{\hat{\varphi}}{2}|0, p\rangle| &\approx 1 - \frac{1}{2}\sqrt{\frac{E_C}{8E_J}} - \frac{3}{64}\frac{E_C}{E_J} \sim 0.9 \approx 1, \\
|\langle 0, p|\sin\frac{\hat{\varphi}}{2}|0, p\rangle| &\approx |\sin(2\pi n_g)|\left(\frac{2}{3}\right)^{2/3}\Gamma\left(\frac{1}{3}\right)\left(\frac{E_C}{8E_J}\right)^{\frac{1}{6}}\frac{\epsilon_i}{\omega_p} \approx 0,
\end{aligned} \tag{D10}$$

where Γ in the last expression is the gamma function.

Inserting Eqs. (D9) and (D10) into Eq. (D8) with the help of Eq. (D6), we obtain

$$\begin{aligned}
\Gamma_{00} &= \frac{32E_J}{h}\frac{1}{\Delta}\int_{\Delta}^{\infty} f_{\rm ne}(1 - f_{\rm ne})d\epsilon \\
&= \frac{16E_J}{h\Delta}\int_{\Delta}^{\infty}\frac{1}{1 + \cosh\left(\frac{\epsilon - \delta\mu}{k_B T}\right)}d\epsilon \\
&= \frac{16E_J k_B T}{h\Delta}\frac{1}{1 + e^{(\Delta - \delta\mu)/k_B T}} \\
&\approx \frac{16E_J k_B T}{h\Delta}\frac{1}{1 + \frac{\mathcal{N}}{n_{\rm qp}}} \approx \boxed{\frac{16E_J k_B T}{\mathcal{N}\Delta h} n_{\rm qp} \equiv K n_{\rm qp}},
\end{aligned} \tag{D11}$$

where we have assumed $n_{\rm qp} \ll \mathcal{N}$ in arriving at the final expression. Equation (7) is thus proven.

APPENDIX E: DIFFUSION AND TUNNELING SIMULATIONS WITHIN THE LEADS

We have made the assumption that the $n_{\rm qp}$ injected into the neighborhood local to the junction thermalizes rapidly and is uniform throughout the trap, motivating the use of a chemical shift. In reality, quasiparticle deposits in the trap take time to diffuse to the junction and tunnel across. We briefly investigated the validity of this prescription, following Ref. [105], by modeling quasiparticle diffusion and tunneling as

$$\frac{\partial u(x, y, t)}{\partial t} = D\nabla^2 u(x, y, t) - \frac{K}{V_{\rm trap}}u(x, y, t)\delta(\vec{r} - \vec{r}_j) - \frac{1}{\tau_{\rm qp}}u(x, y, t). \tag{E1}$$

We assume reflective Neumann boundary conditions and have reduced the problem to two dimensions (as film thickness $\ll$ phonon absorber size). Tunneling is modeled as a delta-function sink term. As in Appendix A, we assume a fixed quasiparticle lifetime, in this case taking $\tau_{\rm qp} = 1$ ms

as a typical value at low quasiparticle density [77]. We use a value of $K \approx 3\ \mathrm{kHz}\,\mu\mathrm{m}^3$ similar to Sec. IV B. V_{tr} is the volume of the junction, and trap dimensions are taken to match this volume, with investigated geometries ranging from square to aspect ratios of $\sim$10. r_j is the location of the junction. $u(x, y, t)$ is normalized to unity such that it can be interpreted as the probability density function of a quasiparticle in the absorber. We set $D = 2\ \mathrm{cm}^2\ \mathrm{s}^{-1}$, assuming that the trap region diffusion is similar to aluminum. Literature values range from $D = 22.5$ to $34\,\mathrm{cm}^2\ \mathrm{s}^{-1}$ [102]. The latter comes from a measurement on 20 nm thick aluminum (thinner than our proposed traps), performed by a subset of authors of this paper, where they extracted the diffusion constant through its relationship to the critical superconducting field H_c as per Ref. [118]. The choice of a much smaller diffusion constant in our simulations comes from certain reports indicating poor diffusion for thin (<100 nm) films [54,100,101].

The instant diffusion limit ($D \to \infty$) solution of Eq. (E1) is equivalent to having the junction be the entire volume of the trap: $\dot{u}(t) = -Ku(t)/V_{\mathrm{tr}} - u(t)/\tau_{\mathrm{qp}}$. The normalized absorber quasiparticle density thus becomes $u(t) = e^{-t/\tau_t} e^{-t/\tau_{\mathrm{qp}}}$, where $\tau_t = V/K$ is the tunneling time. We compare this regime to one with the measured diffusion constant and simulate solutions to Eq. (E1) using standard finite-difference techniques. From this process, we ascertain a few things: (1) Agreement between the simulated solution and the instant diffusion limit justifies our use of a uniform quasiparticle density, n_{qp}, and a chemical potential, $\delta\mu$, across the trap. (2) Quasiparticles become uniformly distributed over the trap regardless of the initial location of the energy deposition (including uniform injection from the sidewall opposite the junction) and aspect ratio. (3) $\tau_{\mathrm{qp}} \ll \tau_t$, so recombination dominates over tunneling. In particular, we can view the tunneling rate as a measure of the trap quasiparticle density. (4) Equation (4), in spite of diffusion, is a good description of the uniform, recombination-dominated quasiparticle density. In totality, the results obtained from the simulation are consistent with the conclusions presented in Sec. III.

APPENDIX F: ABSORBER AND TRAP BALANCE

Here, we show that a source of nonthermal background quasiparticles in the absorber can lead to greatly elevated quasiparticle densities in the trap. A simplified model of the steady-state quasiparticle population within the trap and absorber can be written as set of coupled differential equations. The density in the absorber can be expressed as

$$\frac{dn_{\mathrm{qp,abs}}}{dt} = \frac{1}{V_{\mathrm{abs}}}\left(\Gamma^{\mathrm{abs}}_{\mathrm{gen}} - \Gamma^{\mathrm{abs}}_{\mathrm{rec}}\right) - p\frac{V_{\mathrm{tr}}}{V_{\mathrm{abs}}}\frac{n_{\mathrm{qp,abs}}}{\tau_{\mathrm{tr}}}, \tag{F1}$$

where $\Gamma^{\mathrm{abs}}_{\mathrm{gen,rec}}$ are quasiparticle generation and recombination terms, inclusive of any thermal or pair-breaking radiation contribution. The last term represents the fractional loss into the trap with an assumed trapping timescale τ_{tr} related to the phonon emission timescale (among other considerations). We have introduced a transmission probability in the last term, p, such that with perfect transmission quasiparticles dwell within the trap for time in proportion to the volume of the trap versus the absorber.

The corresponding equation for the trap is

$$\frac{dn_{\mathrm{qp,tr}}}{dt} = \frac{1}{V_{\mathrm{tr}}}\left(\Gamma^{\mathrm{tr}}_{\mathrm{gen}} - \Gamma^{\mathrm{tr}}_{\mathrm{rec}}\right) + p\frac{n_{\mathrm{qp,abs}}}{\tau_{\mathrm{tr}}}\eta_{\mathrm{pb}}\frac{\Delta_{\mathrm{abs}}}{\Delta_{\mathrm{tr}}}, \tag{F2}$$

where the first term corresponds again to quasiparticle generation and recombination and the second term is the source term due to trapping, copied over from the first equation and accounting for the different volume. While experimental input will be required to correctly constrain such a model, we can use reasonable assumptions to evaluate the dynamics. We assume elevated but still very low quasiparticle densities of approximately $\mathcal{O}(0.01)\ \mu\mathrm{m}^{-3}$ in the trap, an $\mathcal{O}(1)$ ms quasiparticle lifetime in the absorber, an $\mathcal{O}(100)$ µs lifetime within the trap, an $\mathcal{O}(100)$ ns trapping timescale, and a constant injection of quasiparticles into the absorber that would, at steady state, result in an absorber density of $\sim$0.05 quasiparticles $\mu\mathrm{m}^{-3}$. We can solve the system of equations, with the

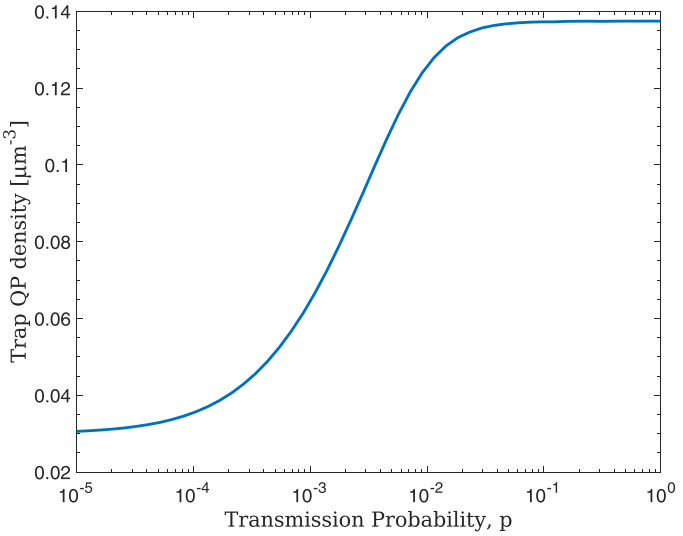


FIG. 14. Trap quasiparticle density as a function of transmission probability from the absorber, for values given in the text. As the capture probability increases, the more elevated the trap density can become at steady state, directly affecting detector sensitivity.

resulting trap density versus transmission probability shown in Fig. 14. We establish our conclusion from Sec. IV B: At steady state, and as the transmission probability improves, the trap quasiparticle density can be greatly elevated from its quiescent value and can be many times larger.

[1] M. Battaglieri *et al.*, US cosmic visions: New ideas in dark matter 2017: Community report, arXiv:1707.04591; R. Kolb *et al.*, Basic research needs for dark-matter small projects new initiatives: Report of the department of energy's high energy pysics workshop on dark matter, Technical Report, USDOE Office of Science (2018), https://www.osti.gov/servlets/purl/1659757/; B. Fleming *et al.*, Basic research needs for high energy physics detector research & development: Report of the Office of Science Workshop on Basic Research Needs for HEP Detector Research and Development: December 11–14, 2019, Technical Report, USDOE Office of Science (2019), https://doi.org/10.2172/1659761.

[2] D. K. Papoulias, T. S. Kosmas, and Y. Kuno, Recent probes of standard and non-standard neutrino physics with nuclei, Front. Phys. **7**, 191 (2019).

[3] R. Essig *et al.*, Snowmass2021 Cosmic Frontier: The landscape of low-threshold dark matter direct detection in the next decade, arXiv:2203.08297.

[4] T. Trickle, Direct detection of light dark matter with electrons, phonons, and magnons, Ph.D. thesis, California Institute of Technology, 2022.

[5] T. Trickle, Z. Zhang, K. M. Zurek, K. Inzani, and S. M. Griffin, Multi-channel direct detection of light dark matter: Theoretical framework, J. High Energy Phys. 03 (2020) 036.

[6] K. D. Irwin, S. W. Nam, B. Cabrera, B. Chugg, and B. A. Young, A quasiparticle-trap-assisted transition-edge sensor for phonon-mediated particle detection, Rev. Sci. Instrum. **66**, 5322 (1995).

[7] J. Rothe *et al.*, TES-based light detectors for the CRESST direct dark matter search, J. Low Temp. Phys. **193**, 1160 (2018).

[8] I. Alkhatib *et al.*, Light dark matter search with a high-resolution athermal phonon detector operated above ground, Phys. Rev. Lett. **127**, 061801 (2021).

[9] C. Fink *et al.*, Characterizing TES power noise for future single optical-phonon and infrared-photon detectors, AIP Adv. **10**, 085221 (2020).

[10] R. Romani, Correlated and uncorrelated backgrounds and noise sources in athermal phonon detectors and other low temperature detector (2023), https://indico.slac.stanford.edu/event/8288/contributions/7765/attachments/3735/10116/Romani_CPAD_2023.pdf.
[11] R. Anthony-Petersen *et al.*, Low energy backgrounds and excess noise in a two-channel low-threshold calorimeter, Appl. Phys. Lett. **126**, 102601 (2025).
[12] O. Wen, T. Aralis, R. Basu Thakur, B. Bumble, Y.-Y. Chang, K. Ramanathan, and S. Golwala, Performance of a phonon-mediated detector using KIDs optimized for sub-GeV dark matter, J. Low Temp. Phys. **209**, 510 (2022).
[13] D. Moore, S. Golwala, B. Bumble, B. Cornell, P. Day, H. LeDuc, and J. Zmuidzinas, Position and energy-resolved particle detection using phonon-mediated microwave kinetic inductance detectors, Appl. Phys. Lett. **100**, 232601 (2012).
[14] D. Delicato *et al.*, Low-energy spectrum of the BULLKID detector array operated on surface, Eur. Phys. J. C **84**, 353 (2023).
[15] Y. Nakamura, Y. A. Pashkin, and J. Tsai, Coherent control of macroscopic quantum states in a single-Cooper-pair box, Nature (London) **398**, 786 (1999).
[16] A. Somoroff, Q. Ficheux, R. A. Mencia, H. Xiong, R. Kuzmin, and V. E. Manucharyan, Millisecond coherence in a superconducting qubit, Phys. Rev. Lett. **130**, 267001 (2023).
[17] C. D. Wilen *et al.*, Correlated charge noise and relaxation errors in superconducting qubits, Nature (London) **594**, 369 (2021).
[18] V. Iaia, J. Ku, A. Ballard, C. Larson, E. Yelton, C. Liu, S. Patel, R. McDermott, and B. Plourde, Phonon downconversion to suppress correlated errors in superconducting qubits, Nat. Commun. **13**, 6425 (2022).
[19] A. Bargerbos, L. J. Splitthoff, M. Pita-Vidal, J. J. Wesdorp, Y. Liu, P. Krogstrup, L. P. Kouwenhoven, C. K. Andersen, and L. Grünhaupt, Mitigation of quasiparticle loss in superconducting qubits by phonon scattering, Phys. Rev. Appl. **19**, 024014 (2023).
[20] J. M. Martinis, Saving superconducting quantum processors from decay and correlated errors generated by gamma and cosmic rays, npj Quantum Inf. **7**, 90 (2021).
[21] M. McEwen *et al.*, Resisting high-energy impact events through gap engineering in superconducting qubit arrays, Phys. Rev. Lett. **133**, 240601 (2024).
[22] M. D. Shaw, R. M. Lutchyn, P. Delsing, and P. M. Echternach, Kinetics of nonequilibrium quasiparticle tunneling in superconducting charge qubits, Phys. Rev. B **78**, 024503 (2008).
[23] G. Catelani, Parity switching and decoherence by quasiparticles in single-junction transmons, Phys. Rev. B **89**, 094522 (2014).
[24] G. Catelani, R. J. Schoelkopf, M. H. Devoret, and L. I. Glazman, Relaxation and frequency shifts induced by quasiparticles in superconducting qubits, Phys. Rev. B **84**, 064517 (2011).
[25] M. D. Shaw, J. Bueno, P. Day, C. M. Bradford, and P. M. Echternach, Quantum capacitance detector: A pair-breaking radiation detector based on the single Cooper-pair box, Phys. Rev. B **79**, 144511 (2009).
[26] J. Bueno, M. Shaw, P. Day, and P. Echternach, Proof of concept of the quantum capacitance detector, Appl. Phys. Lett. **96**, 103503 (2010).
[27] P. M. Echternach, B. J. Pepper, T. Reck, and C. M. Bradford, Single photon detection of 1.5 THz radiation with the quantum capacitance detector, Nat. Astron. **2**, 90 (2018).
[28] P. M. Echternach, A. D. Beyer, and C. M. Bradford, Large array of low-frequency readout quantum capacitance detectors J. Astron. Telesc. Instrum. Syst. **7**, 011003 (2021).
[29] R. Linehan, I. Hernandez, D. J. Temples, S. Q. Dang, D. Baxter, L. Hsu, E. Figueroa-Feliciano, R. Khatiwada, K. Anyang, D. Bowring, G. Bratrud, G. Cancelo, A. Chou, R. Gualtieri, K. Stifter, and S. Sussman, Estimating the energy threshold of phonon-mediated superconducting qubit detectors operated in an energy-relaxation sensing scheme, Phys. Rev. D **111**, 063047 (2025).
[30] C. W. Fink, C. Salemi, B. A. Young, D. I. Schuster, and N. A. Kurinsky, Superconducting quasiparticle-amplifying transmon: A qubit-based sensor for meV-scale phonons and single terahertz photons, Phys. Rev. Appl. **22**, 054009 (2024).
[31] S. Chowdhury, M. Hays, S. R. Jha, K. Serniak, T. P. Orlando, J. A. Grover, and W. D. Oliver, Theory of quasiparticle generation by microwave drives in superconducting qubits, Phys. Rev. Appl. **25**, 014042 (2026).

[32] P. J. de Visser, J. J. A. Baselmans, S. J. C. Yates, P. Diener, A. Endo, and T. M. Klapwijk, Microwave-induced excess quasiparticles in superconducting resonators measured through correlated conductivity fluctuations, Appl. Phys. Lett. **100**, 162601 (2012).
[33] D. Goldie and S. Withington, Non-equilibrium superconductivity in quantum-sensing superconducting resonators, Supercond. Sci. Technol. **26**, 015004 (2013).
[34] K. Serniak, M. Hays, G. De Lange, S. Diamond, S. Shankar, L. Burkhart, L. Frunzio, M. Houzet, and M. Devoret, Hot nonequilibrium quasiparticles in transmon qubits, Phys. Rev. Lett. **121**, 157701 (2018).
[35] J. Koch, M. Y. Terri, J. Gambetta, A. A. Houck, D. I. Schuster, J. Majer, A. Blais, M. H. Devoret, S. M. Girvin, and R. J. Schoelkopf, Charge-insensitive qubit design derived from the Cooper pair box, Phys. Rev. A **76**, 042319 (2007).
[36] S. Knapen, T. Lin, M. Pyle, and K. M. Zurek, Detection of light dark matter with optical phonons in polar materials, Phys. Lett. B **785**, 386 (2018).
[37] R. Essig, M. Fernandez-Serra, J. Mardon, A. Soto, T. Volansky, and T.-T. Yu, Direct detection of sub-GeV dark matter with semiconductor targets, J. High Energy Phys. 05 (2016) 046.
[38] A. Shnirman, G. Schön, and Z. Hermon, Quantum manipulations of small Josephson junctions, Phys. Rev. Lett. **79**, 2371 (1997).
[39] Y. Y. Gao, M. A. Rol, S. Touzard, and C. Wang, Practical guide for building superconducting quantum devices, PRX Quantum **2**, 040202 (2021).
[40] N. Booth, Quasiparticle trapping and the quasiparticle multiplier, Appl. Phys. Lett. **50**, 293 (1987).
[41] D. Goldie, N. Booth, C. Patel, and G. Salmon, Quasiparticle trapping from a single-crystal superconductor into a normal-metal film via the proximity effect, Phys. Rev. Lett. **64**, 954 (1990).
[42] S.-H. Kim *et al.*, Development of superconducting tunnel junction photon detector using hafnium, Phys. Procedia **37**, 667 (2012).
[43] S. Kraft, A. J. Peacock, M. Bavdaz, B. Castelletto, B. Collaudin, D. Perez, R. Venn, and T. E. Harper, Use of hafnium-based superconducting tunnel junctions as high-resolution spectrometers for x-ray astronomy, in *EUV, X-Ray, and Gamma-Ray Instrumentation for Astronomy IX*, Proc. SPIE 3445 (SPIE, 1998), pp. 226–235.
[44] A. Wallraff, D. I. Schuster, A. Blais, L. Frunzio, R.-S. Huang, J. Majer, S. Kumar, S. M. Girvin, and R. J. Schoelkopf, Strong coupling of a single photon to a superconducting qubit using circuit quantum electrodynamics, Nature (London) **431**, 162 (2004).
[45] J. Q. You and F. Nori, Superconducting circuits and quantum information, Phys. Today **58**(11), 42 (2005).
[46] P. Krantz, M. Kjaergaard, F. Yan, T. P. Orlando, S. Gustavsson, and W. D. Oliver, A quantum engineer's guide to superconducting qubits, Appl. Phys. Rev. **6**, 021318 (2019).
[47] In the CPB case, the parity shift is interpreted as a change in the device capacitance (hence quantum capacitance detector).
[48] J. Aumentado, M. W. Keller, J. M. Martinis, and M. H. Devoret, Nonequilibrium quasiparticles and 2e periodicity in single-Cooper-pair transistors, Phys. Rev. Lett. **92**, 066802 (2004).
[49] J. Burnett, A. Bengtsson, D. Niepce, and J. Bylander, in Noise and loss of superconducting aluminium resonators at single photon energies, J. Phys. Conf. Ser. **969**, 012131 (2018).
[50] K. Ramanathan *et al.*, Significant noise improvement in a Kinetic Inductance Phonon-Mediated detector by use of a wideband parametric amplifier, arXiv:2402.05419.
[51] T. Connolly, P. D. Kurilovich, S. Diamond, H. Nho, C. G. L. Bøttcher, L. I. Glazman, V. Fatemi, and M. H. Devoret, Coexistence of nonequilibrium density and equilibrium energy distribution of quasiparticles in a superconducting qubit, Phys. Rev. Lett. **132**, 217001 (2024).
[52] S. B. Kaplan, C. C. Chi, D. N. Langenberg, J. J. Chang, S. Jafarey, and D. J. Scalapino, Quasiparticle and phonon lifetimes in superconductors, Phys. Rev. B **14**, 4854 (1976).
[53] M. C. Pyle, Optimizing the design and analysis of cryogenic semiconductor dark matter detectors for maximum sensitivity, Ph.D. thesis, Stanford University, 2012.
[54] C. W. Fink, A gram-scale low-Tc low-surface-coverage athermal-phonon sensitive dark matter detector, Ph.D. thesis, University of California, Berkeley, CA, 2022.

[55] T. Saab, Search for weakly interacting massive particles with the cryogenic dark matter Search experiment, Ph.D. thesis, Stanford University, 2002.
[56] R. Ren *et al.*, Design and characterization of a phonon-mediated cryogenic particle detector with an eV-scale threshold and 100 keV-scale dynamic range, Phys. Rev. D **104**, 032010 (2021).
[57] S. R. Golwala and E. Figueroa-Feliciano, Novel quantum sensors for light dark matter and neutrino detection, Annu. Rev. Nucl. Part. Sci. **72**, 419 (2022).
[58] T. K. Bui *et al.*, First limits on light dark matter interactions in a low threshold two-channel athermal phonon detector from the TESSERACT collaboration, Phys. Rev. Lett. **135**, 161002 (2025).
[59] O. Wen, Strategic planning and sensitivity-enhancing tactics for detecting low-mass particle dark matter with phonon-mediated detectors, Ph.D. thesis, California Institute of Technology, 2025.
[60] T. Guruswamy, D. Goldie, and S. Withington, Quasiparticle generation efficiency in superconducting thin films, Supercond. Sci. Technol. **27**, 055012 (2014).
[61] A. Kozorezov, A. Volkov, J. Wigmore, A. Peacock, A. Poelaert, and R. Den Hartog, Quasiparticle-phonon downconversion in nonequilibrium superconductors, Phys. Rev. B **61**, 11807 (2000).
[62] In some literature, e.g., Ref. [64], this is itself called the phonon collection efficiency.
[63] With feature sizes still able to be optically lithographed.
[64] D. J. Temples *et al.*, Performance of a phonon-mediated kinetic inductance detector at the NEXUS cryogenic facility, Phys. Rev. Appl. **22**, 044045 (2024).
[65] M. Pyle *et al.*, Surface electron rejection from Ge detector with interleaved charge and phonon channels, in *The Thirteenth International Workshop on Low Tempertaure Detectors–LTD13*, AIP Conf. Proc. No. 1185 (American Institute of Physics, Melville, New York, 2009), pp. 223–226.
[66] L. Cardani, N. Casali, I. Colantoni, A. Cruciani, S. Di Domizio, M. Martinez, V. Pettinacci, G. Pettinari, and M. Vignati, Final results of CALDER: Kinetic inductance light detectors to search for rare events, Eur. Phys. J. C **81**, 636 (2021).
[67] A. Cruciani *et al.*, BULLKID: Monolithic array of particle absorbers sensed by kinetic inductance detectors, Appl. Phys. Lett. **121**, 213504 (2022).
[68] J. Zotova, S. Sanduleanu, G. Fedorov, R. Wang, J. S. Tsai, and O. Astafiev, Control and readout of a transmon using a compact superconducting resonator, Appl. Phys. Lett. **124**, 102601 (2024).
[69] B. Foxen *et al.*, Qubit compatible superconducting interconnects, Quantum Sci. Technol. **3**, 014005 (2018).
[70] K. Satzinger *et al.*, Simple non-galvanic flip-chip integration method for hybrid quantum systems, Appl. Phys. Lett. **114**, 173501 (2019).
[71] R. K. Romani, Y.-Y. Chang, R. Mahapatra, M. Platt, M. Reed, I. Rydstrom, B. Sadoulet, B. Serfass, and M. Pyle, A transition edge sensor operated in coincidence with a high sensitivity athermal phonon sensor for photon coupled rare event searches, Appl. Phys. Lett. **125**, 232601 (2024).
[72] G. Angloher *et al.*, Quasiparticle diffusion in CRESST light detectors, J. Low Temp. Phys. **184**, 323 (2016).
[73] R. A. Moffatt, Two-dimensional spatial imaging of charge transport in germanium crystals at cryogenic temperatures, Ph.D. thesis, Stanford University, 2016.
[74] S. W. Leman, Invited review article: Physics and Monte Carlo techniques as relevant to cryogenic, phonon, and ionization readout of Cryogenic Dark Matter Search radiation detectors, Rev. Sci. Instrum. **83**, 091101 (2012).
[75] R. Barends, J. Baselmans, S. Yates, J. Gao, J. Hovenier, and T. Klapwijk, Quasiparticle relaxation in optically excited high-Q superconducting resonators, Phys. Rev. Lett. **100**, 257002 (2008).
[76] P. J. de Visser, J. Baselmans, J. Bueno, N. Llombart, and T. Klapwijk, Fluctuations in the electron system of a superconductor exposed to a photon flux, Nat. Commun. **5**, 3130 (2014).
[77] J. Zmuidzinas, Superconducting microresonators: Physics and applications, Annu. Rev. Condens. Matter Phys. **3**, 169 (2012).
[78] J. Baselmans and S. Yates, Long quasiparticle lifetime in aluminum microwave kinetic inductance detectors using coaxial stray light filters, in *The Thirteenth International Workshop on Low Tempertaure Detectors–LTD13*, AIP Conf. Proc. No. 1185 (American Institute of Physics, Melville, New York, 2009), pp. 160–163.

[79] O.-P. Saira, A. Kemppinen, V. F. Maisi, and J. P. Pekola, Vanishing quasiparticle density in a hybrid Al/Cu/Al single-electron transistor, Phys. Rev. B **85**, 012504 (2012).
[80] D. Ristè, C. Bultink, M. J. Tiggelman, R. N. Schouten, K. W. Lehnert, and L. DiCarlo, Millisecond charge-parity fluctuations and induced decoherence in a superconducting transmon qubit, Nat. Commun. **4**, 1913 (2013).
[81] Y.-Y. Chang, SuperCDMS HVeV Run 2 low-mass dark matter search, highly multiplexed phonon-mediated particle detector with kinetic inductance detector, and the blackbody radiation in cryogenic experiments, Ph.D. thesis, California Institute of Technology, 2023.
[82] J. M. Martinis and K. Osborne, Superconducting qubits and the physics of Josephson junctions, arXiv:cond-mat/0402415.
[83] K. Serniak, S. Diamond, M. Hays, V. Fatemi, S. Shankar, L. Frunzio, R. Schoelkopf, and M. Devoret, Direct dispersive monitoring of charge parity in offset-charge-sensitive transmons, Phys. Rev. Appl. **12**, 014052 (2019).
[84] R. Lutchyn, L. Glazman, and A. Larkin, Quasiparticle decay rate of Josephson charge qubit oscillations, Phys. Rev. B **72**, 014517 (2005).
[85] R. Lutchyn and L. Glazman, Kinetics of quasiparticle trapping in a Cooper-pair box, Phys. Rev. B **75**, 184520 (2007).
[86] D. Averin and K. Likharev, Coulomb blockade of single-electron tunneling, and coherent oscillations in small tunnel junctions, J. Low Temp. Phys. **62**, 345 (1986).
[87] Because of the density of states singularity at Δ, it is reasonable to assume all nonequilibrium quasiparticles in the absorber reside at the gap energy.
[88] V. Manucharyan, Superinductance, Ph.D. thesis, Yale University, 2012.
[89] P. Echternach, K. Stone, C. Bradford, P. Day, D. Wilson, K. Megerian, N. Llombart, and J. Bueno, Photon shot noise limited detection of terahertz radiation using a quantum capacitance detector, Appl. Phys. Lett. **103**, 053510 (2013).
[90] Assuming that the absorber in this case is an unspecified higher-gap material like α-Ta or Nb.
[91] D. Baxter, R. Essig, Y. Hochberg, M. Kaznacheeva, B. von Krosigk, F. Reindl, R. K. Romani, and F. Wagner, Low-energy backgrounds in solid-state phonon and charge detectors, Annu. Rev. Nucl. Part. Sci. **75**, 301 (2025).
[92] N. Zobrist, B. Ho Eom, P. Day, B. A. Mazin, S. R. Meeker, B. Bumble, H. G. LeDuc, G. Coiffard, P. Szypryt, N. Fruitwala, I. Lipartito, and C. Bockstiegel, Wide-band parametric amplifier readout and resolution of optical microwave kinetic inductance detectors, Appl. Phys. Lett. **115**, 042601 (2019).
[93] P. J. de Visser, J. J. A. Baselmans, P. Diener, S. J. C. Yates, A. Endo, and T. M. Klapwijk, Generation-recombination noise: The fundamental sensitivity limit for kinetic inductance detectors, J. Low Temp. Phys. **167**, 335 (2012).
[94] U. Fano, Ionization yield of radiations. II. The fluctuations of the number of ions, Phys. Rev. **72**, 26 (1947).
[95] P. Verhoeve, N. Rando, A. Peacock, A. Van Dordrecht, A. Poelaert, and D. Goldie, Superconducting tunnel junctions as photon counting detectors in the infrared to the ultraviolet, IEEE Trans. Appl. Supercond. **7**, 3359 (1997).
[96] L. V. Abdurakhimov, I. Mahboob, H. Toida, K. Kakuyanagi, Y. Matsuzaki, and S. Saito, Identification of different types of high-frequency defects in superconducting qubits, PRX Quantum **3**, 040332 (2022).
[97] O. Noroozian, J. Gao, J. Zmuidzinas, H. G. LeDuc, and B. A. Mazin, Two-level system noise reduction for microwave kinetic inductance detectors, in *The Thirteenth International Workshop on Low Tempertaure Detectors–LTD13*, AIP Conf. Proc. No. 1185 (American Institute of Physics, Melville, New York, 2009), pp. 148–151.
[98] T. Saab, R. Clarke, B. Cabrera, R. Abusaidi, and R. Gaitskell, Design of QET phonon sensors for the CDMS ZIP detectors, Nucl. Instrum. Methods Phys. Res., Sect. A **444**, 300 (2000).
[99] B. A. Mazin, Superconducting materials for microwave kinetic inductance detectors, in *Handbook of Superconductivity*, edited by D. A. Cardwell, D. C. Larbalestier, and A. Braginski (CRC Press, Boca Raton, Florida, 2022), pp. 756–765.

[100] J. J.-C. Yen, Phonon sensor dynamics for Cryogenic Dark Matter Search experiment: A study of quasiparticle transport in aluminum coupled to tungsten transition edge sensors, Ph.D. thesis, Stanford University, 2015.

[101] J. Yen, J. Kreikebaum, B. A. Young, B. Cabrera, R. Moffatt, P. Redl, B. Shank, P. Brink, M. Cherry, and A. Tomada, Quasiparticle transport in thick aluminum films coupled to tungsten transition edge sensors, J. Low Temp. Phys. **184**, 30 (2016).

[102] S. Hsieh and J. L. Levine, Diffusion of quasiparticles in superconducting aluminum films, Phys. Rev. Lett. **20**, 1502 (1968).

[103] Y. Dong, Y. Li, W. Zheng, Y. Zhang, Z. Ma, X. Tan, and Y. Yu, Measurement of quasiparticle diffusion in a superconducting transmon qubit, Appl. Sci. **12**, 8461 (2022).

[104] N. Kurinsky, The low-mass limit: Dark matter detectors with eV-scale energy resolution, Ph.D. thesis, Stanford University, 2018.

[105] C. Wang, Y. Y. Gao, I. M. Pop, U. Vool, C. Axline, T. Brecht, R. W. Heeres, L. Frunzio, M. H. Devoret, G. Catelani, L. I. Glazman, and R. J. Schoelkopf, Measurement and control of quasiparticle dynamics in a superconducting qubit, Nat. Commun. **5**, 5836 (2014).

[106] M. Masuzawa, K. Tsuchiya, A. Terashima, A. Dael, O. Napoly, and J. Plouin, Magnetic shielding our experience with various shielding materials, in *Proceedings of SRF2013, Paris, France* (Joint Accelerator Conferences Website (JACoW), Geneva, 2013), pp. 808–811.

[107] M. H. Kelsey *et al.*, G4CMP: Condensed matter physics simulation using the Geant4 toolkit, Nucl. Instrum. Methods Phys. Res., Sect. A **1055**, 168473 (2023).

[108] M. Martinez, L. Cardani, N. Casali, A. Cruciani, G. Pettinari, and M. Vignati, Measurements and simulations of athermal phonon transmission from silicon absorbers to aluminum sensors, Phys. Rev. Appl. **11**, 064025 (2019).

[109] M. McEwen *et al.*, Resolving catastrophic error bursts from cosmic rays in large arrays of superconducting qubits, Nat. Phys. **18**, 107 (2022).

[110] D. Rosenberg *et al.*, 3D integrated superconducting qubits, npj Quantum Inf. **3**, 42 (2017).

[111] J. Goupy, J. Colas, M. Calvo, J. Billard, P. Camus, R. Germond, A. Juillard, L. Vagneron, M. De Jesus, F. Levy-Bertrand, and A. Monfardini, Contact-less phonon detection with massive cryogenic absorbers, Appl. Phys. Lett. **115**, 223506 (2019).

[112] G. Angloher *et al.*, Results on sub-GeV dark matter from a 10 eV threshold CRESST-III silicon detector, Phys. Rev. D **107**, 122003 (2023).

[113] J. Collar, Search for a nonrelativistic component in the spectrum of cosmic rays at Earth, Phys. Rev. D **98**, 023005 (2018).

[114] A. Rothwarf and B. Taylor, Measurement of recombination lifetimes in superconductors, Phys. Rev. Lett. **19**, 27 (1967).

[115] B. Palmer, C. Sanchez, A. Naik, M. Manheimer, J. Schneiderman, P. Echternach, and F. Wellstood, Steady-state thermodynamics of nonequilibrium quasiparticles in a Cooper-pair box, Phys. Rev. B **76**, 054501 (2007).

[116] C. Owen and D. Scalapino, Superconducting state under the influence of external dynamic pair breaking, Phys. Rev. Lett. **28**, 1559 (1972).

[117] J. M. Martinis, M. Ansmann, and J. Aumentado, Energy decay in superconducting Josephson-junction qubits from nonequilibrium quasiparticle excitations, Phys. Rev. Lett. **103**, 097002 (2009).

[118] J. M. Gordon and A. Goldman, Electron inelastic scattering in aluminum films and wires at temperatures near the superconducting transition, Phys. Rev. B **34**, 1500 (1986).